A Passive Optical Proximity Sensor

by

Ashish Rai

B.Tech., Symbiosis International University, 2017

Thesis Submitted in Partial Fulfillment of the
Requirements for the Degree of
Master of Applied Science

in the
School of Mechatronic Systems Engineering
Faculty of Applied Science

© **Ashish Rai 2019**
SIMON FRASER UNIVERSITY
Fall 2019

Approval

Name:	**Ashish Rai**
Degree:	**Master of Applied Science**
Title:	**A Passive Optical Proximity Sensor**

Examining Committee: **Chair:**   Amr Marzouk
Lecturer

Behraad Bahreyni
Senior Supervisor
Associate Professor

Gary Leach
Supervisor
Associate Professor

Michael Adachi
Internal Examiner
Assistant Professor
School of Engineering Science

Date Defended: **November 25, 2019**

Abstract

A new optical proximity sensor was developed and studied in this project. A 3D printed model is used for proving the concept. An integrated model with a new geometry was then microfabricated to further improve the sensor model's performance. The sensing operation is based on measurement of light intensity falling on photodiodes placed at an inclined angle with respect to the base surface of the sensor. A mathematical model and subsequent experiments prove that it is possible to determine the distance between a light source and the sensor. This sensor is operated passively which means it does not need an active emission for range sensing. The sensor shows reliable operation for short range proximity detection in the range of 5-15 cm. The sensor structure is pyramidal placed flat on the surface with a fixed base angle. Two independent photodiodes are formed on two of the opposite sides of the pyramid. One such pyramid pixel is able to measure the light intensity and the angle at which the light is incident towards the sensor. Using the intensity measured by micro-fabricated test pyramids structures, the distance to the light source is measured. The experimental values demonstrate that the measurements are accurate and repeatable, more so, the device utilizes no active emission to attain proximity measurements. The discussed device can be used for close and continuous proximity detection in mobile devices with low power consumption.

Keywords: Proximity Sensor, Photodiode, Light Sensing, optical, microfabrication

Table of Contents

List of Figures

Chapter 1

Introduction

1.1 Background and Motivation

In this day and age image perception and 3D mapping have become an integral part of environmental sensing or object detection mechanism. The latest smartphones have multiple cameras that are capable of capturing 2D as well as 3D images. Typical approaches to achieve 3D imaging include structured light imaging [1], ultrasound depth sensing [2], time of flight based sensing [3, 4], stereo photogrammetry [5] and LiDAR [6]. These methods have limited applications that best fit the sensor's nature of operation. However, scientists and engineers every day try to push the boundaries of proximity sensing capabilities by developing application-specific techniques targeting low power consumption, ease of use, a higher level of data abstraction and better resolution.

A simple way of increasing the resolution of a device that can capture 2D image is to increase the number of pixels or measuring points that the device measures when capturing a single sample image. However, to achieve accurate depth sensing with low power consumption and high resolution using the same device becomes challenging. It is possible to employ techniques such as changing differential focal length captures, measuring the shift in an object, and projecting points to measure depth among many other ways for proximity sensing.

There are a number of techniques applied in image capture and surround sensing. One such sensor that is specifically used in sensing applications is a proximity sensor [7]. Proximity sensors have found application in robotic human-machine interfaces, prostheses, and vehicular parking sensors among many other fields. The industrial applications of range detection sensors vary by resolution and range requirements. Some applications where a high dynamic range is critical are discussed in [8, 9], precision applications which need high resolution are discussed in [10, 11, 12].

An increase in reliance on sensors translates into high power usage and complicated design. This signals an imminent need for passive, low power proximity sensing mechanisms. This document discusses how an optical sensor can use incident light to estimate the angle to a light source and how this can further be extended to triangulate the distance to a distant light emitting object.

1.2   Outline of the Thesis

This work presents a novel way of proximity detection using a microfabricated light based proximity sensor. This document provides an overview of the background, model, tests and inferences related to the sensor.

The **Literature Review** section discusses previously popular and currently used proximity sensing models and also some fundamental components used and studied for this work. This chapter further delves into miniaturizing of sensors and discusses their application and relevance in the industry.

The next chapter is **Vector Light Sensors**. In this chapter the sensor's 3D prototype model, operation and basic structure is presented. The device's use in different environments its application and range capabilities are also discussed. An important part of this study discusses noise and error measurements of the sensor and how it becomes increasingly important to keep the signal noise at a minimum for accurate distance measurements.

Microfabricated Vector Light Sensor shows the design concepts and operation principles that lead to forming a single chip with microstructures that are used for passive proximity detection to distant objects. The rationale for the mask design and a brief discussion of the fabrication steps are discussed. The experiments section presents multiple test approaches and theories related to the device's operation and limits.

The **Experimental Results** provide proof of operation of the sensor, discusses measurement results for the discrete and integrated pyramidal models. This shows that the sensor is repeatable and the mathematical model is accurate. The measurement setup and device images are also presented in this section.

The last chapter, **Conclusion and Future Works** summarizes the operation principles, tests, and results. Contribution to the scientific community, specifically in the field of proximity sensing is highlighted. Some ideas on the future work and relevant application of the proposed sensor is discussed.

Chapter 2

Literature Review

This chapter discusses industrial and commercially used proximity sensors and sensing mechanisms. Proximity Sensing refers to detection and measurement of the distance to nearby objects without physical contact. Such techniques have been in existence for decades in fields such as consumer electronics, defense, automotive, food processing, and manufacturing industries. Multiple types of proximity sensors relying on ultrasonic, infrared, magnetic and capacitive interfaces cater to the vast need for proximity sensing mechanisms.

The proximity sensors' market is expanding with growth in demand from applications that rely on proximity sensing. Sensor-based technologies such as infotainment systems, multimedia enhancements, 3-Dimensional gesture recognition system along with other control systems used in consumer electronics has attracted a lot of audiences. Based on the sensor application, the market is further segmented into categories such as automotive, robotics and manufacturing industry.

Manufacturing is a key task in the consumer product industry. Manufacturers produce a variety of products from raw materials in the form of metal, ore, wood, oil, and fabrics. Resource extraction and subsequent processes involves a lot of labor and mostly repetitive tasks. Such an environment serves as a suitable breeding ground for robots [13, 14, 15, 16]. Automation has started to become commonplace in the manufacturing and service industries. Advancements in robotics are critical in driving this change. Companies are investing more time and money into developing technology than manpower which has enabled man to create jobs that never existed 20 years ago.

Another popular application of sensors is to maintain a safe working environment in industries. Machines in industries are equipped with advanced sensors such as strain [17], chemical [18] and other non-contact proximity sensors. Specific sensors or combinations of sensors are used to meet the application's requirement. Sensors provide an analog or digital output which serves as a decision-making tool for the interrogating system. A sensor with a

binary output is referred to as a detector. Proximity detectors can be used in places where, for instance, an obstruction in the sensor's field of view can trigger an immediate shut down in case of an emergency [19].

Catering to complex tasks and performance requirements need sophisticated sensors that efficiently extract information from their surrounding environment and provide reliable information to the parent robot to act safely.

2.1 Proximity Detection

For a binary output, the input detection mechanism can be thought of as a relay switch [20]. When certain conditions are met, the switch is closed, or the output is 'yes'. Such a sensor would need a defined threshold to which the sensor would respond and produce the output. Because the output is just one bit, proximity detection can be achieved without having a complex sensor design.

2.2 Proximity Sensing

Proximity Sensing is a non-contact means of measuring the distance to an object that is in the sensor's field of view. The proximity sensor market has grown exponentially in the last decade and simultaneously the need for sensors has also increased [21]. The literature discussed touches a versatile group of sensing mechanisms and the following chapters are based on the new optical sensor model that can similarly be used in proximity sensing.

2.2.1 Vision based proximity sensing

Camera

Camera is a common instrument used in image and video capturing. Cameras today have built in artificial intelligence, auto focus and auto adaption features that provide real time image and video processing. Their utility in multiple applications has made cameras desirable for use in robotic applications along with other fields such as its use in consumer electronics and defense.

In robotics, vision perception has become an effective practice as image processing algorithms have continued to advance. In [22] the authors have discussed swarm robotics that suggests use of smaller robots rather than one large size robot. Multiple smaller robots allow better space utilization and also makes it easier to detect and perform maintenance on individual robots while not affecting the entire system. The robots are able to perform on-board image processing using cameras fitted on their chassis.

A multiple camera model robotic vehicle is discussed in [23]. Color-depth cameras as discussed in [24] are widely used in robotic applications. Inspired by 3D imaging the work describes a method to accurately calibrate the depth-sensing camera to meet industrial robotics standards. Possibility of unforeseen situations where incorrect decision based on the senor reading cost huge manufacturing damage, injure the workers around the robot or cause machine stalling deem the resolution and accuracy in image processing for such applications extremely important and desirable.

Infrared Proximity Sensor

Infrared sensor is an electronic sensing element that employs infrared radiations (IR) for detecting the target object. The Infrared waves are invisible to the eye and can travel long distances. Infrared radiation lies between the visible and millimeter wave region in the electromagnetic spectrum with wavelength (λ) between 0.75 and 1000μm.
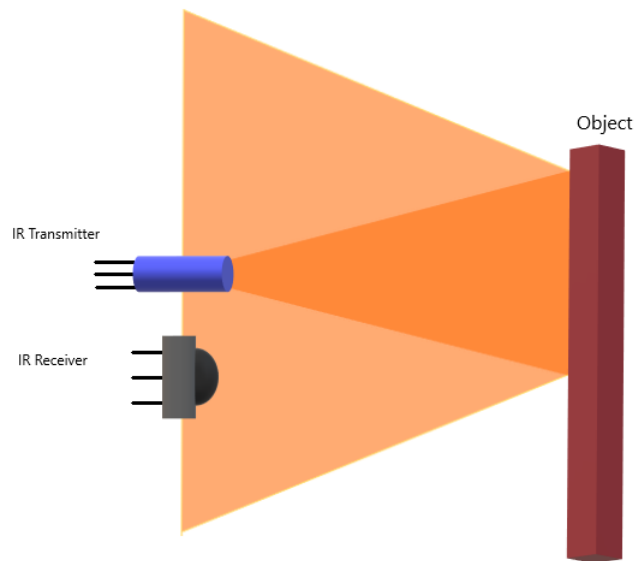
Figure 2.1: Infrared sensor in presence and absence of an object in its field of view.

The infrared spectrum can be split into near IR, mid-IR and far IR. The wavelength region from 0.75 to 3μm is known as the near-infrared region. The region between 3 and 6μm is known as the mid-infrared region, and infrared radiation which has a wavelength greater higher than 6μm is known as far-infrared.

IR waves can also be used in thermal detection [25]. The human body for instance emits infrared waves which can be detected by sensitive IR receivers. In [26] Shieh et al., discuss human robot interaction and single or multiple body estimation using a camera and IR

sensor fusion. The authors also discuss depth estimation using the same setup and employ it in a decision making system for robotic motions.

Infrared sensing is widely used as a in robotics for object recognition, collision detection, path navigation among others that help in active perception of the robot's surrounding. Work done in [27] discusses infrared sensor mounted on a gripper and used for robotic feedback control.

Structured Light Sensor

An interesting proximity sensor which applies concepts based on illumination and light patterns into light field data extraction is a structured light sensor. Structured light is used in applications such as robotics, manufacturing [28], visual inspection [29], structural analysis [30] and haptic response in games [31]. In [32] the authors classify image ranging based on active and passive light projection.

The active light projection technique uses a camera and a pattern projector in tandem, to estimate proximity to the target object based on the continuous image captures. This requires sophisticated image processing and geometric interpolation in real time with dynamically changing surrounding environment. The passive projector ranging technique is based on finding a relation between images taken from the same object surface.

For both techniques, a light projector is used for information extraction. The projector projects a structured light pattern on the object. A light source illuminates an array of spots in the scene. A detector looks towards the scene through a mask which is also facing the distant object in the scene. The mask is arranged in a way that light from a target at a certain range can be uniformly captured.

Structured light's application in 3D surface imaging are discussed in [33]. As shown in figure 2.2 a projector illuminates a 3D object in the scene and this illumination is performed in a pre-structured 2D pattern. Further, a camera is used to capture the 2D image of the illuminated scene. For any difference in the 3D structure of the target object, the projected light pattern would change and the 2D captured image will show discontinuity in the pattern. This distortion is proportional to the height measurement of the object. When calibrated this 2D image based on the structural distortion will give 3D information for the captured image. This image can further be improved by using different light patterns and more complex algorithm so that all aspects of the 3D structured are captured by the camera.
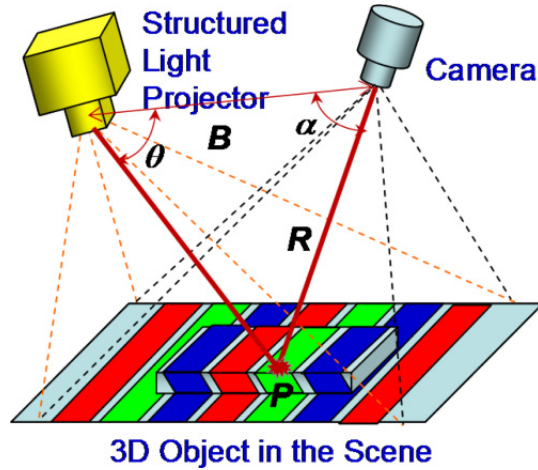
Figure 2.2: Structured Light Camera used to capture features of a 3D object in the space using an RGB striped mask pattern. R is the distance between the target object and the camera, θ is the angle at which the light is projected on the object. α is the angle at which light strikes back from the object and is received by the camera. Source: Adapted from [33] © 2011 Optical Society of America

Optical Time of Flight Sensing

Time of Flight is a phenomenon that uses time difference between signal transmission and reflection from an object for measuring distance to this object. The Time of Flight Camera uses minimal computation and has a simple operating principle [34]. A single frame of image can be captured by a light burst and the resultant depth map gives a fair amount of detail of the target object in the scene. The image provides range information along with intensity information for each captured pixel.

The work in [35] discusses image segmentation and tracking for Time of Flight data. This work also relates the problems with image segmentation and tracking with energy losses and discusses ways to minimize it. Another work [36] discusses Time of Flight sensor technology for people tracking. Here a top-down view of the scene is used to slice the target image, this slicing is based on the probability density and histogram of the captured data. This image information and extraction algorithm provides sufficient data for most situations but needs a more complex algorithm for special cases.

A time-of-flight camera [37] is a range imaging camera system that employs time of flight method to resolve distance between the camera and the subject.

Laser imaging, Detection, and Ranging (LiDAR)

Laser imaging, Detection, and Ranging (LiDAR) [38] is another kind of imaging instrument that shoots pulses of laser light through a transmitter at a very high frequency for capturing 3D image [39, 40]. The receiver in the same housing waits for the pulse to bounce

back and once received records the time required by the pulse to travel this distance. Using this information and because light travels at a constant speed it is possible to locate the distance of an obstructing object in the environment to the sensor. Because this is done at a high frequency, LiDAR can create a 3D image of its surrounding by mapping these reflected points as a function of time it took to return to the receiver. This makes the LiDAR a bulky instrument with a fairly complex dynamic mechanism [41]. Due to the dynamic nature of the image capturing in LiDAR, the relative position of the LiDAR in space becomes critical in determining the data integrity.

Such sensors are widely used in autonomous vehicle technology for 3D imaging of the vehicle's immediate surrounding and to detect potential threats for collision. LiDAR in [42] has been used in tandem with a sensor system for car detection. This approach also used deep learning for projecting the vehicle's future positions based on the current speed and environmental conditions. This approach gives multiple outcomes for the vehicle's future position and a smart system enables the car to make an optimal decision in real-time. The work in [43] discusses LiDAR's use in car following systems to maintain a safe distance between to cars and avoid collisions. LiDAR along with monocular vision study the car's environment and calibrate the LiDAR to provide accurate 3D distance information relative to the other card. This helps in implementing speed control system in the autonomous vehicle.

2.2.2   Ultrasound proximity sensor

Ultrasound sensing has been used for proximity and ranging applications for decades. The operation of ultrasonic sensor involves emitting an ultrasonic pulse at 40kHz frequency or higher. This pulse travels through the air towards the distant object, bounces back, and is received by the sensor.

A typical ultrasonic sensor's operation can be seen in figure 2.3. The time difference in the transmission and reception of the signal can be used to find the distance between the source and the distant object using the following formula [44]:

$$D = \frac{\Delta t V}{2}$$

where, Δt is the time taken by the pulse to reach the target object and back, and V is the velocity of sound in air.

Ultrasonic Sensors can be used for obstacle detection. Many commercially available designs have a maximum operating range of up to 9 -12 meters. These sensors are accurate for near object detection and can provide samples at a high frequency, however, if the object is too
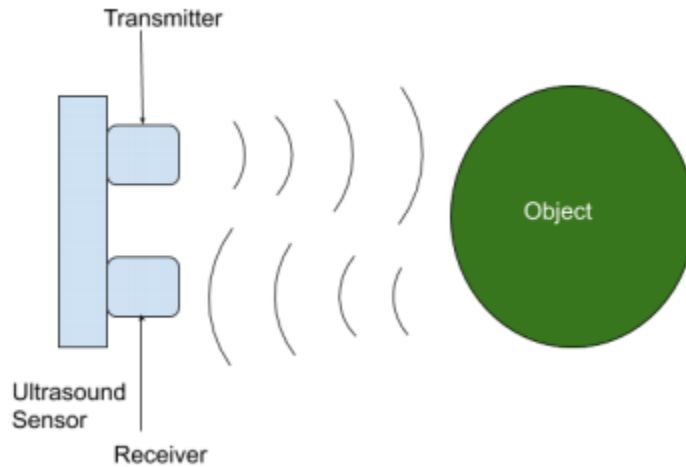
Figure 2.3: Ultrasound sensor with transmitter and receiver mounted next to each other. The waves hit and bounce back from the object which is used in estimating distance between the sensor and the object.

close to the sensor the ultrasonic sensor may not be able to measure its distance. An off the shelf ultrasonic proximity sensor HCSR04 [45] has a dead band of approximately $2cm$. This gap is the region where the transmitter shoots a pulse of waves but the object is so close to the sensor that the waves disperse into the air and none of it is received by the receiver module.

Indoor mobile robots can interact with the surrounding through ultrasonic sensors [46]. Surrounding obstacles are classified into categories and is discerned based on the echo received from the ultrasonic sensing module. The application of ultrasonic sensor can also be extended to object avoidance [47], motion pattern recognition and many more.

Work done in [48] discusses sensor fusion using ultrasonic sensor. The technique used aims at developing an efficient proximity detection mechanism using multiple sensors. The data from the ultrasonic and infrared sensors are compared and fitted by a polynomial. The data is then validated and the performance characteristics are reported. The IR sensor can provide accurate results on the object's relative position in the environment. However, they are ineffective when translucent or transparent objects, mirror or water droplet show up in the sensor's field of view. This is when the robot can rely on the sound based results from the ultrasonic sensor.

Multiple ultrasonic sensors have also been used in a single robot for measuring shapes and features [49]. This makes it possible for the sensor system to get a complete view of its surrounding.

2.2.3 Magnetic Proximity Sensor

Magnetic proximity sensors are non-contact devices that are used for proximity detection using an artificially generated magnetic field. Vicinity to the magnets will disrupt the magnetic field which is used in measuring range and direction to a target ferromagnetic object. Magnetic Sensors can measure the total magnetic field and also determine the vector components of the target in the magnetic field. The paper [50] discusses magnetic sensors and
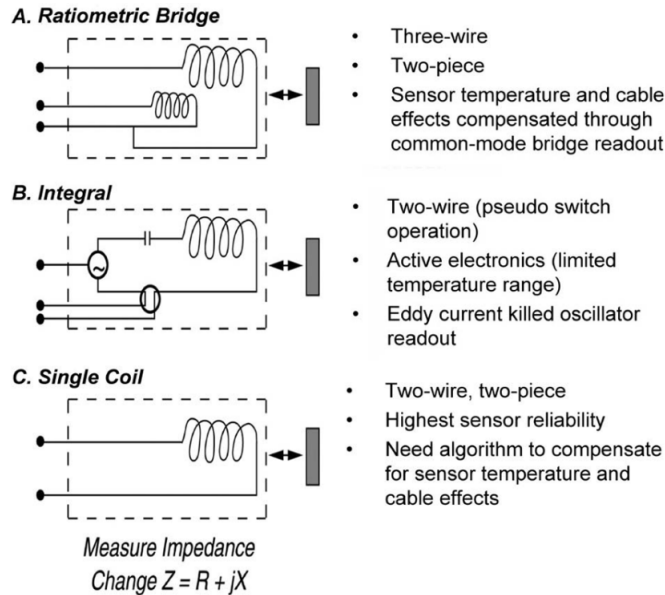
Figure 2.4: Proximity sensing mechanism for metallic objects: (a)resonant circuit method, (b) bridge method, (c) single-coil method. Source: Adapted from [50] © 2006 IEEE

their applications. Figure 2.4 shows three different ways to use a vector search coil magnetometer. Search coil magnetometer works on Faraday's law of Induction of magnetic flux change [51]. The first method as shown in figure 2.4(a) illustrates a balanced inductive bridge and the differential voltage output based on the inductance change is used to determine the object's proximity to the sensor. The second method as shown in figure 2.4(b) is determining proximity based on change in resonant frequency which is again dependent on change in inductance. The third method is a single coil approach where the inductive sensor simply gives out the inductance and there are external electronics that calibrate and compensate temperature losses for the readouts. This is shown in figure 2.4(c).

Magnetic sensing has been used in robotics for proximity detection [52]. A robot is used to detect ferromagnetic objects in its surrounding by using passive magnetic field. This method even though not the best in resolution give a robust alternative to cameras used in robots with on board sensors operating at a high speed [53, 54, 55, 56].

2.2.4 Capacitive Proximity Sensor

Non-contact capacitive sensing derives a target object's features and position when this object is within the sensing electric field of the sensor. Interaction between this field and the object can be modeled to find the location of the object in space. Further this field information can be recorded using an array of such sensors and in different permutations of the array elements to get a better perception of the target's features.

Work in [57] and [58] discuss a capacitive sensing system that is used in industrial human-robot-interactions. This includes information capture using multiple electrode connection configurations in an array embedded in a system guided by a complex digital logic. Further the data is processed using machine learning algorithms. The conductors play an important role in forming the fringing electric field between sense and drive electrodes.

The authors in [59] discuss robotic assistance for differently abled people using a capacitive sensing system. The multidimensional capacitive sensing estimates a human limb position passively and in real time. The sensors can be embedded into clothes or fabric, however the experiments show the use of this sensor when used as a robot's end effector. The limb's position estimates are trained for specific activities using a neural network model and then a feedback control guides the locomotion of the limb to perform these specific activities. Another work [60] exemplifies the use of capacitive sensors using flexible printed circuit boards [61] for recognizing locomotion transition of amputees. They integrate the capacitive sensor with other on-prosthesis mechanical sensors which is proposed as an effective alternative to robotic transtibial prosthesis [62].

2.3 Micromachined Proximity Sensors

Complex proximity sensor designs in the form of a translated amalgamation of simpler sensing models has gained popularity due to higher resolution capabilities. This calls for miniaturizing of sensors to accommodate a greater number of on-board sensors with low power utilization.

2.3.1 Capacitive Micromachined Ultrasonic Transducer

Commercially available ultrasonic tranducers are based on piezo-electric transceivers whereas Capacitive Micromachined Ultrasonic Transducers (CMUT) operate based on electrostatic transduction. These micro transducers allow transmitting and receiving signals in the ultrasonic range. They offer advantages such as wider bandwidth, simple fabrication and higher sensitivity when compared with its piezoelectric counterparts. CMUT find application in fields such as automoubiles, medical instruments, manufacturing, defense among others that are used in proximity measurements and activity tracking.

CMUT operates on the principle of a moving parallel plate capacitor. An AC voltage is applied to the membrane which causes the membrane to vibrate, sending out an ultrasound signal. When receiving this signal, the vibration of the membrane results in change in capacitance which is calibrated into a distance measurement unit for measuring proximity. Figure 2.5 illustrates how the sensor works [63].
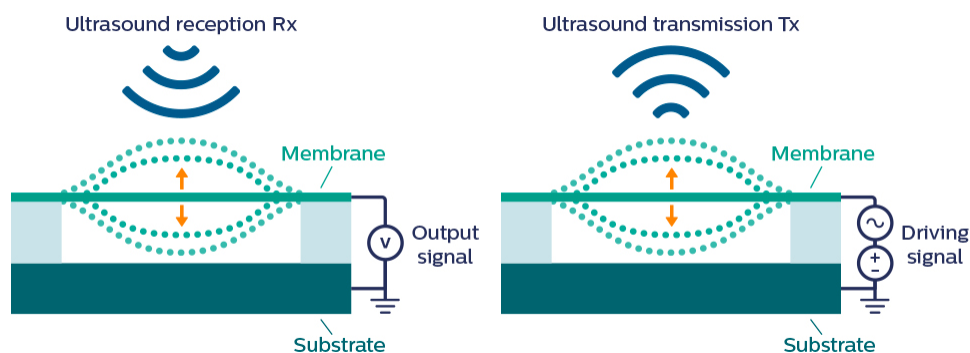
Figure 2.5: Working principle of CMUT sensor showing both the receiver and transmitter side of the communication. Source: Figure adapted from [63]

Authors in [64] discuss CMUT's application in ultrasonic ranging. They claim that CMUT can be highly sensitive which allows them to be used in systems requiring a high Signal-to-Noise ratio. CMUT provides a high dynamic range of operation and can circumvent attenuation problems of ultrasonic waves when propagating in air. The experimental results show successful operation of the sensor in detecting ultrasonic waves through an aluminum block. This test is performed for up to a 100dB dynamic range.

Photoacoustic imaging is a biomedical medical imaging method based on photoacoustic effect [65]. Work shown in [66] uses 3D photo-acoustic imaging using a CMUT array. When light is pulsed through a biological tissue, it is absorbed by chromophores which release a wideband ultrasonic wave. The CMUT captures these waves to attain photoacoustic images. CMUT is used in short range but high resolution proximity detection and imaging.

2.3.2   Millimeter Wave Radar Proximity Sensing

Millimeter Wave Radar uses short wavelength electromagnetic waves which are transmitted and then reflected back from objects in the field of view and are received back by the receiver. Such an approach provides the position of the object in 3D space and also allows motion tracking. An antenna's dimensions is related to its signal wavelength. For millimeter wave, that means it's less than a couple of millimeters across. This allows for having smaller and lighter micro-fabricated antennas. Unlike previously discussed proximity de-

tection techniques such as LiDAR and cameras, millimeter wave radar can be used in bad weather conditions (fog, rain, low visibility areas) which allows these sensors to be used in vehicles for navigation and guidance [67]. An array of millimeter wave radars can perform simultaneous operations to provide a wide angular view to the operator.

Autonomous land navigation vehicles need robust and accurate sensors to perform efficiently in all sorts of road and weather conditions. Work [68] discusses millimeter wave radar's use and performance in such autonomous cars. The authors illustrated a test vehicle with radar and GPS system [69] mounted on the car's roof. Vehicle navigation is performed using multiple sensors and Extended Kalman Filter algorithm [70]. All the captured data is then used to create a navigation map for the vehicle, based on which the vehicle makes critical driving decisions. Work done by Google, an engineering technology company, has resulted in a gesture sensing device called 'Soli' which uses millimeter wave radar for motion detection in embedded devices. This gesture sensing technology can sense proximity and motion with a sub-millimeter accuracy [71] which can greatly improving the capability of consumer electronics.

This chapter lays ground for future chapters by discussing some of the developed proximity sensing technologies in the market. Proximity sensing is a widely researched topic and has applications in fields such as autonomous driving technology, consumer electronics, smart devices among many others. The future chapters discuss a novel optical based proximity sensor - the device model, fabrication and test results.

Chapter 3

Vector Light Sensor

This chapter discusses light sensing, modeling, and simulations targeted at being able to attain light field information using a sensor that can measure angle and light intensity of the incident light and use this to triangulate the proximity to the object. An object in 3D space blocks background light which makes the shape and size of this object noticeable. Studying how the pattern of light received changes can lead to identifying the characteristics of this object. Light detection techniques have matured as the applications of such sensors in fields such as robotics, communication, Internet of Things among many others, have exponentially increased.

While discussing the sensor, its design and applications, some introductory concepts about light field information and data extraction are explained. Further, multiple such pixels can be used for gaining higher levels of abstraction from the surrounding environment and the same information can be extracted using different geometries or designs of this sensor.

3.1 Device Model - Vector Light Sensor

Vector light sensor uses a pyramidal structure as shown in figure 3.1 to estimate the light angle with respect to the surface. A light sensor is used to measure the incident light intensity. The light sensor is placed on inclined surfaces with respect to the surface. Experiments and the model discussed use a pyramid which has 4 sidewalls and the base angle or angle of inclination of the light sensor is denoted by α.

By using two light sensors on inclined, opposite, and symmetric pyramid sidewalls, it is now possible to estimate not only the magnitude but also angle at which the light illuminates the surface.

$$
\begin{aligned}
P_{E_{incident}} &= A_s \cdot \mathfrak{I}_{in} \cdot \sin(\beta + \alpha) \\
P_{W_{incident}} &= A_s \cdot \mathfrak{I}_{in} \cdot \sin(\beta - \alpha)
\end{aligned}
\tag{3.1}
$$

Based on equation 3.1, the ratio of power from light from East and West fixed light sensors is:

$$R_{P_E/P_W} = \frac{\sin(\beta + \alpha)}{\sin(\beta - \alpha)} \tag{3.2}$$

Solving equation 3.2 for β [72] gives:

$$\beta = \alpha - \arctan\left(\frac{R_{P_E/P_W} \cdot \cos(2\alpha) - 1}{R_{P_E/P_W} \cdot \sin(2\alpha)}\right) \tag{3.3}$$

The value β derived in equation 3.3 is the angle of incidence with respect to surface.
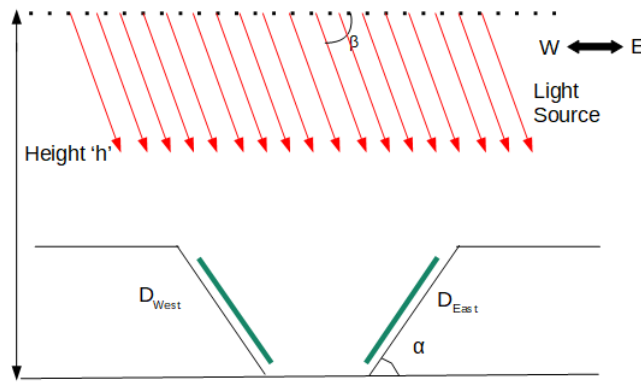
Figure 3.1: Angle estimation parameters for a planar light source falling on an inverted pyramid sensor which has two inclined side walls labeled D_East and D_West

A novelty of this approach is that for a given β, even though the generated photo-current changes with irradiated light intensity, the ratio of intensities : R_{P_E/P_W}, remains constant which makes the sensor immune to light of varying intensities.

The current discussion suggests a way to measure the angle at which light is shining with respect to the surface. Going a step further, it is possible to record multiple such source angles β_x from the same base surface to triangulate distance to a light source in space.

To ascertain the angular position of a light source is critical to this sensing model. A single pyramid structure that can detect angle to the light source is the primary element of range sensing mechanism - as would also be discussed in future chapters. Accurate angular estimation is critical because this would result in low error in the measured angle.

A photodiode [73] is used as a light sensor in testing the Vector Light Sensor model.

3.2 Photodiode

A photodiode is a semiconductor light sensing device that absorbs incident photons and converts it into an electrical current. The current generated is proportional to absorbed photons by the photodiode. Photodiodes have a PN junction, called so because it formed between a P and N type semiconductor [74]. Under the influence of an applied voltage across the diode, a depletion region is formed by the PN junction. For a positive voltage across the PN junction, the diode starts to become forward biased [75], the forward voltage for a typical silicon diode is 0.7V. The depletion region is thicker when the diode is reverse biased and thinner when the diode is forward biased. For performed experiments and models discussed in the future chapters, the diode is zero biased, which means the P side of the diode is connected to ground. In this case, only dark current, and photo generated current [76] can flow through the diode.

Diodes form an essential part of this proximity sensor. Tests have been performed on commercially available photodiodes BPW34 and on in-house micro-fabricated photodiodes. The BPW34s can be seen in figure 3.2. A photodiode is so called because of its responsiveness to incident photons. For a constant voltage drop in the reverse biased mode, with increase in light incident on the diode the conductivity of the diode starts increasing. This mode of operation for a diode is called photoconductive mode. A typical diode equation is given by:

$$I_d = I_0 \cdot \left(e^{\frac{qV}{nK_bT}} - 1 \right) + I_p \tag{3.4}$$

where, I_d is the net current flowing through the diode, I_0 is the dark saturation current, which is the diode leakage current measured with no light, q is the electric charge, V is the applied voltage across the terminals of the diode, K_b is Boltzmann's constant, I_p is the net photo current changing with change in light intensity, T is absolute temperature (in Kelvin), and n is the ideality factor, usually between 1 and 2. For operating voltages before the breakdown, when a diode is reverse biased the only variable that changes is I_p, that is the current due to change in light intensity.

3.3 Data Acquisition

The photodiode connected in the circuit as shown in figure 3.3 generates a current in the inverting input leg of the opamp. A transimpedance amplifier converts input current to voltage readable by a data acquisition system. The transimpedance amplifier used with appropriate gain R_f helps to ensure that the opamp does not saturate but at the same time

Figure 3.2: Photodiodes used on macro-model sensor device

maintains its resolution to show a significant change in voltage value with change in light intensity falling on the photodiode.
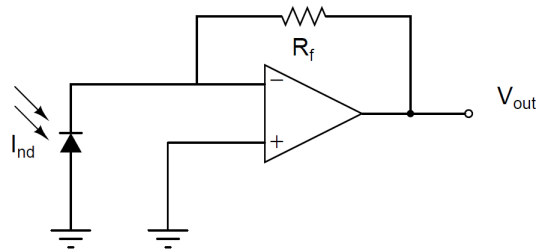
Figure 3.3: Data capture using a photodiode in a transimpedance amplifier circuit

Figure 3.3 shows a photodiode in zero bias connected to the inverting terminal of the op amp. Based on the light intensity, there is an equivalent photocurrent I_{nd} generated which is fed to the inverting input of the op amp. Depending on the range of voltage output that we are operating on we can adjust the gain R_f and get the desired amplification. In no light condition or inside a dark room there is no current flowing through the diode and all we see at the output is random signal variations. When light is incident on the photodiode, current starts flowing and we see a change in the output voltage. The output voltage can be calculated by using Kirchhoff's Current Law [77], the sum of input currents is equal to the sum of output currents. The sensitivity of the circuit can be increased by using a higher

17

gain resistor.

The power of irradiated light on the diode placed on a flat surface is:

$$P_{incident} = A_s \cdot \mathfrak{I}_{in} \cdot \sin(\beta) \tag{3.5}$$

where, A_s is the area of photodiode surface, $\mathfrak{I}_{in}$ is the incident light intensity, and β is the angle at which light is incident on the diode.

3.4 Proximity Sensing using Pyramid Structures

The previous section discussed height measurements when two β values are recorded from different points on the same surface. In this section, the design model for extracting these β values is discussed.

3.4.1 Bi-Pyramid Proximity Detection

A bi-pyramid approach uses two pyramid structures next to each other. Each pyramid has two light sensors that sit on two of the opposite facing sidewalls of each pyramid. Having multiple light sensors as arranged in figure 3.4 allows estimating two angles β_1 and β_2 from different locations on the surface.
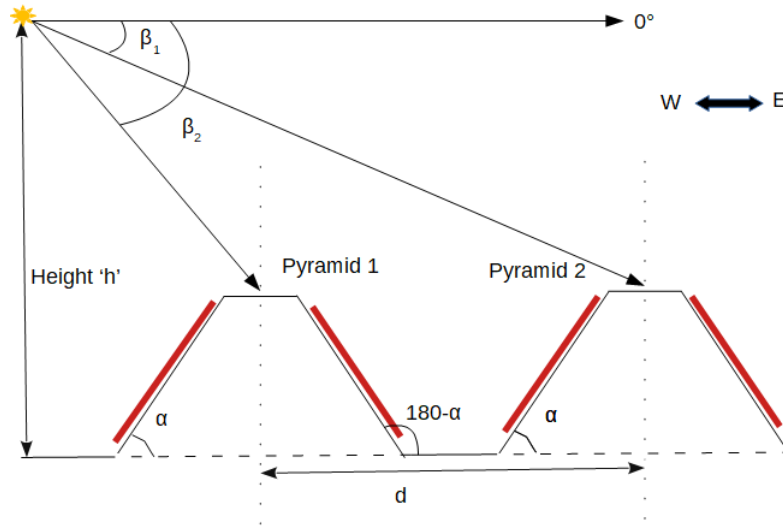
Figure 3.4: A bi pyramid model with light sensors (marked in red) fixed on opposite facing pyramid sidewalls, where 'd' is the inter-pyramid distance, 'h' is the height from the pyramid base to the light source.

As illustrated in figure 3.4, β_1 and β_2 show the angle at which light is incident on the sensor; distance 'd' shows the distance between two pyramids which is constant; height 'h' can be

18

found by using the formula:

$$h = \frac{d}{|\cot(\beta_2) - \cot(\beta_1)|} \tag{3.6}$$

Placing two pyramids next to each other allows for the possibility of incident light measurement errors due to reflection between two diodes that are facing each other. This would negatively impact the angular measurements from both the pyramids and would finally also affect the height measurements.

3.4.2 Single Pyramid Proximity Detection

It is possible to create a single, fused, off-centered, tilted pyramid structure. This new structure occupies the space of one pyramid and uses three photo sensors. However, the structure allows the pyramid to be decomposed into two individual pyramids. Each pyramid can sense angle β with a modified formula 3.7. This can be used to find the distance to the light source. This techniques allows better space utilization on the chip surface.
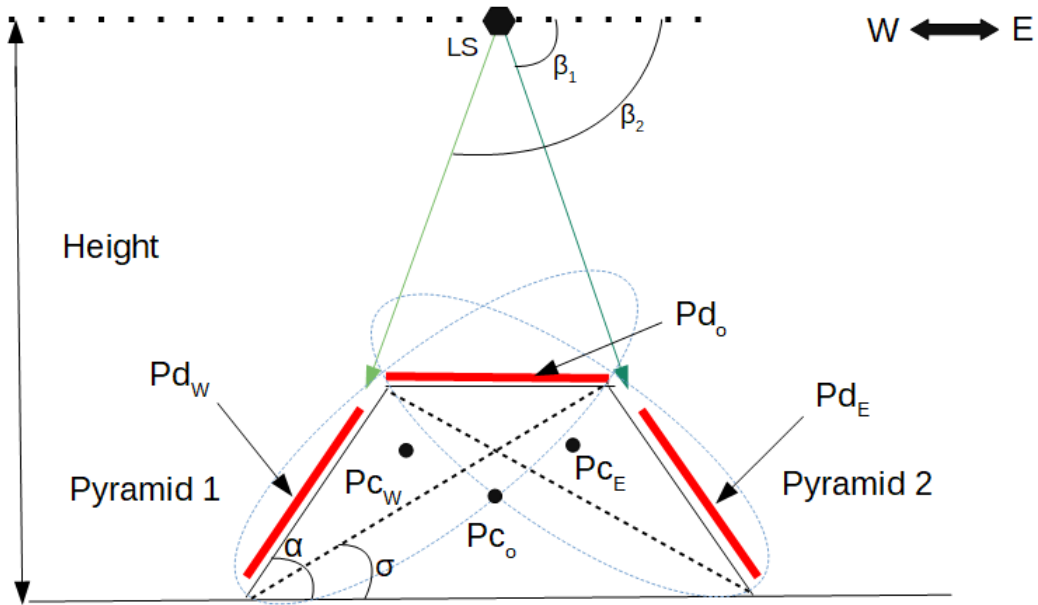
Figure 3.5: A fused pyramid model where one pyramid structure can be virtually divided into two individual pyramids. P_{dW} and P_{dO} form pair 1, P_{dE} and P_{dO} form pair 2 that result in two pyramids. σ is the angle with which the pyramids are offset with respect to surface.

Figure 3.5 shows 3 photodiodes as marked Pd_E, Pd_W, and Pd_O. These photodiodes are independent from each other and have similar characteristics. The area marked pyramid 1 and pyramid 2 are two individual pyramids formed out of the available three photo sensors. These pyramids share photodiode Pd_O which lies flat on top of the structure. The center for pyramid 1 it labeled as Pc_E and for pyramid 2 as Pc_W. These points are important

19

because the measured angle β is calculated from these points. There is a third center Pc_O which is the center of the whole pyramid. This is used to find a third reference angle which is used for calibrating β_1 and β_2 . This can also be used to find a third β which can further improve the height measurement accuracy. The formula for calculating β is:

$$\beta_x = -\sigma + \alpha - \arctan\left(\frac{R_{P_E/P_W} \cdot \cos(2\alpha) - 1}{R_{P_E/P_W} \cdot \sin(2\alpha)}\right) \tag{3.7}$$

This approach would not face inter-pyramid reflection problems as discussed in the bi-pyramid model. However, instead of having 4 independent diodes, now the model has one shared diode between to pyramids.

3.5 Noise Estimates and Measurement simulations

For two pyramids overlapping each other completely, the estimated angle at which light is irradiated would be the same. If one of the pyramids is moved in any of the directions in the plane, this measured angle will be different for the two pyramids. However, the difference in estimation will be almost constant because the two pyramids are next to each other, and the position of the pyramid is the reference point of angular estimations to the given light source.
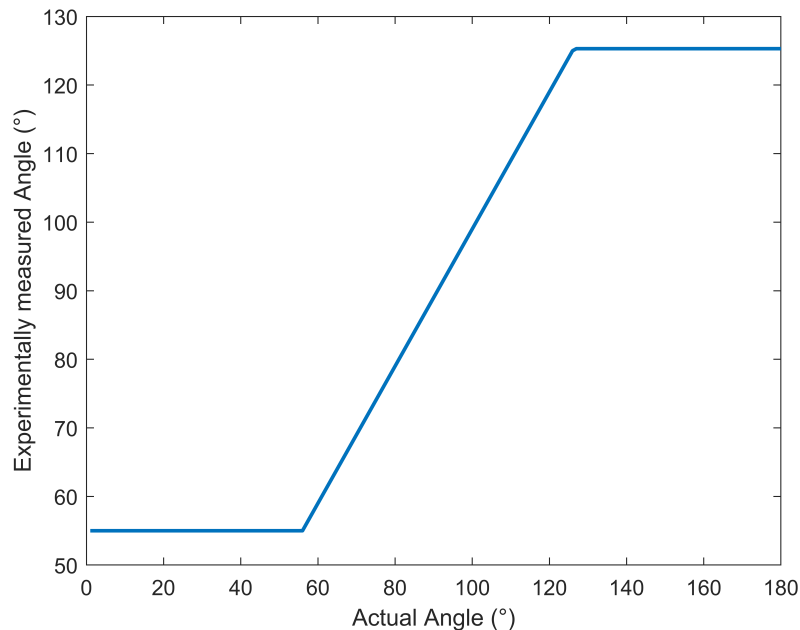
Figure 3.6: Estimated angle plot for real incident angles on the sensor versus the estimated angle by the sensor. The flat region shows the region that is out of the field of view of this sensor.

As shown in figure 3.6, the angular measurements for an ideal sensor would give a linear and proportional response for input incident light irradiation angles. Because of the physi-

cal structure of the sensor, the viewing angle of the sensor allows reliable estimations for a window of $+\alpha$ to $\pi - \alpha$. Beyond these values one of the photodiodes would not be receiving any light from the source.

There are certain external factors that affect the sensor's performance and appear as noise at the sensor output. The major noise contributions can be modelled and included in the angular calculations. These include:

1. Thermal Noise

2. Shot Noise

3. Op-Amp Noise

These noise sources affect the circuit's performance and if they are dominant enough, they can be comparable to the the actual signal output. This brings in more complexities in data acquisition, filtering, and analysis.

A noise model for the data acquisition system consists of a current/voltage source that is responsible for the specific noise contribution source. Figure 3.7 shows a model for data acquisition used for capturing the sensor's output. The circuit also shows the noise sources which are replaced by individual current/voltage sources.
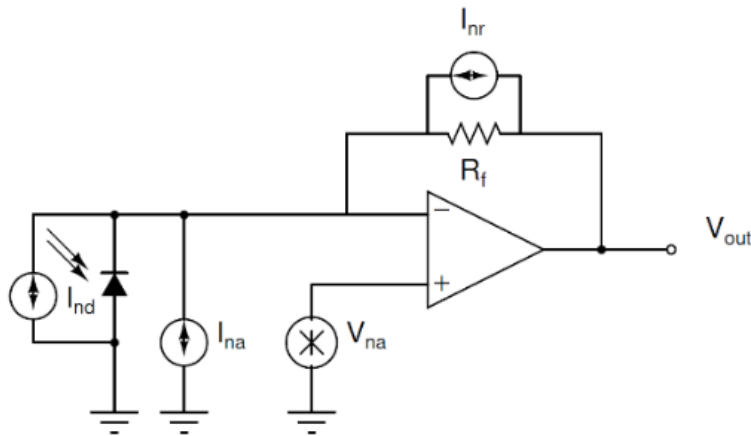
Figure 3.7: Transimpedance amplifier with a photodiode which is zero biased. The current and voltage sources shown are noise sources in the circuit. I_{nd} is the shot noise across diode, I_{na} is the amplifier input current noise, V_{na} is the amplifier input voltage noise, I_{nr} is the thermal noise in Rf

3.5.1   Thermal Noise

The thermal noise in a circuit is generated due to charge carrier agitation in a conductor. The charge carrier agitation increases with increase in temperature which increases the

21

thermal noise. In figure 3.7 thermal noise is marked as a current source in parallel with the feedback resistor. The equation for Thermal noise is:

$$i_{nr} = \sqrt{\frac{4 \cdot K_b \cdot BW \cdot T}{R_f}} \tag{3.8}$$

where i_{nr} is the RMS of the thermal current noise, BW is the bandwidth in Hz, i.e., the frequency bounds of the system. For a pre-defined feedback resistor value and assuming room temperature, the thermal noise is as shown in the figure 3.8.
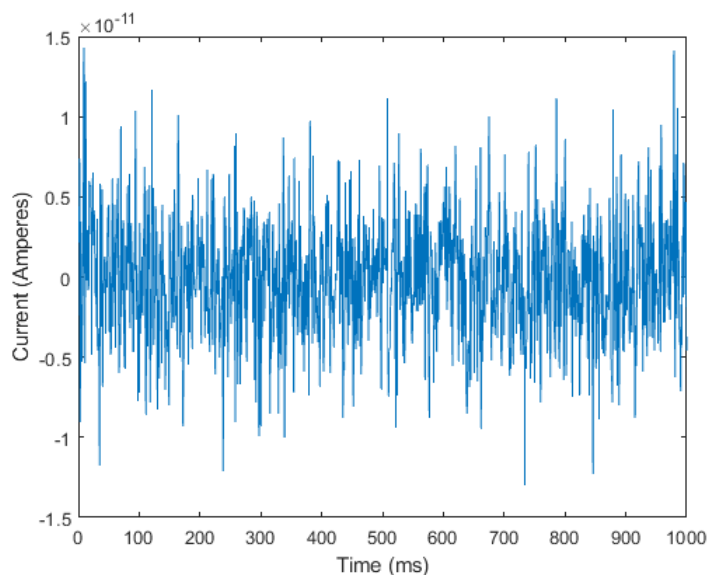
Figure 3.8: Thermal noise contribution to the amplifier circuit. The X axis shows time and the Y axis shows the estimated current noise in the circuit.

3.5.2 Shot Noise

Shot noise is caused by fluctuation in current values from its mean. It does not depend on system temperature as in the case of Thermal Noise. The flow of current through a diode makes it critical to consider shot noise as a major noise contributor in the system's noise equation. Shot noise is represented by adding a current source in parallel with the diode as shown in the noise model figure 3.7.

The equation for contributed shot noise is:

$$i_{nd} = \sqrt{2 \cdot q \cdot I_{DM} \cdot BW} \tag{3.9}$$

where, i_{nd} is the diode current noise, q is the charge of an electron, I_{DM} is the average DC current through the diode. The estimated shot noise is calculated and is shown in figure 3.9.
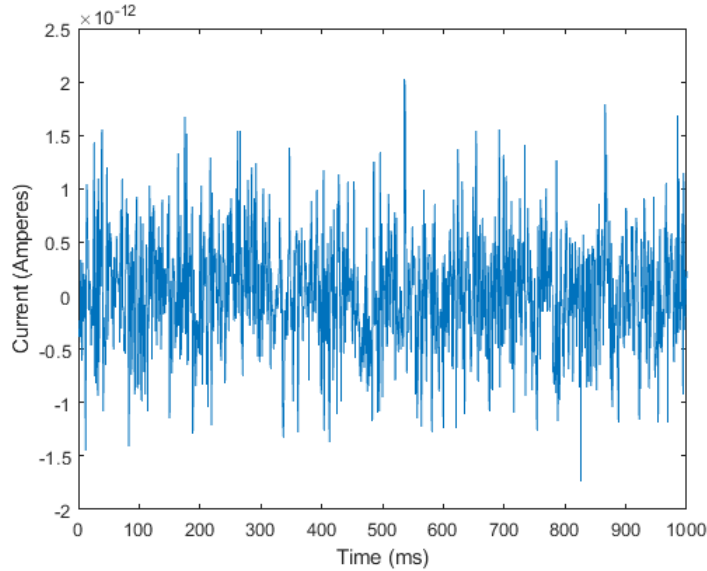
Figure 3.9: Shot noise contribution to the amplifier circuit. The X axis shows time and the Y axis shows the estimated current noise in the circuit.

3.5.3 Op-Amp Noise

Noise generated in opamp is different from noise generated from its circuit interface. The Op-Amp used here is a low noise amplifier but the noise effect can still be significant and a good benchmark to compare other noise components with. The Op-Amp noise can be modeled by both input current and voltage noise sources. The equivalent input noise sources for an op-amp are indicated in figure 3.7 as I_{na} and V_{na} respectively.

3.5.4 Total Noise Contribution and Comparison

Total noise is a contribution of all individual noise sources as shown in figure 3.7. All the noise sources are replaced by equivalent current source so that they are comparable when their in value with the other noise sources and the input. The op-Amp noise is inherent, however, because the value R_f is high, the thermal resistance dominates. As illustrated in figure 3.10, the magnitude of different noise sources are compared by plotting the output fluctuations on the same plot.

The equation for total noise at the output is given by:

$$V_{ntotal} = \sqrt{\left(R_f{}^2 \cdot (i_{nd}^2 + i_{na}^2 + i_{nr}^2) + v_{na}^2\right) \cdot BW} \tag{3.10}$$

V_{ntotal} is the noise portion of the V_{out} that is shown in figure 3.7. This includes thermal, op-amp and shot noises, which are converted into total noise voltage at the output. There are other noise sources that can show up within the bandwidth of operation of the sensor,
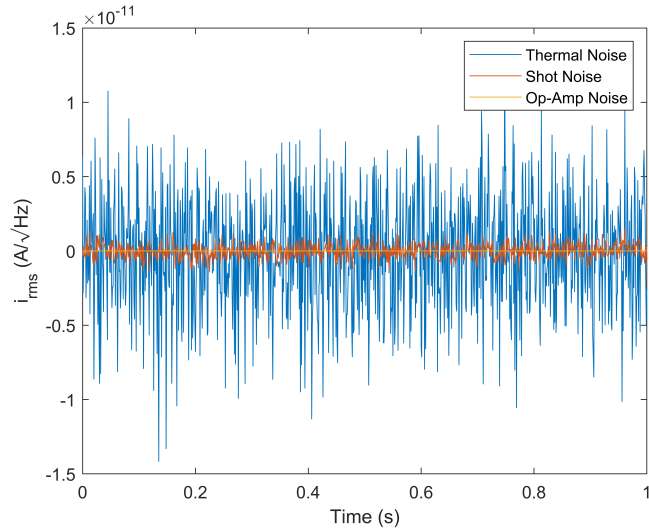
Figure 3.10: Total noise contribution from thermal, shot and op-Amp Noise

however, we need the sensor to provide an output of light intensity that can be used to find a relation with the current flowing through the diode. For an ideal diode the dark current can be in the range of a few nano amperes and the noise level is insignificant when compared with the actual signal. The smallest detectable signal is often limited by noise when the two signals become comparable.
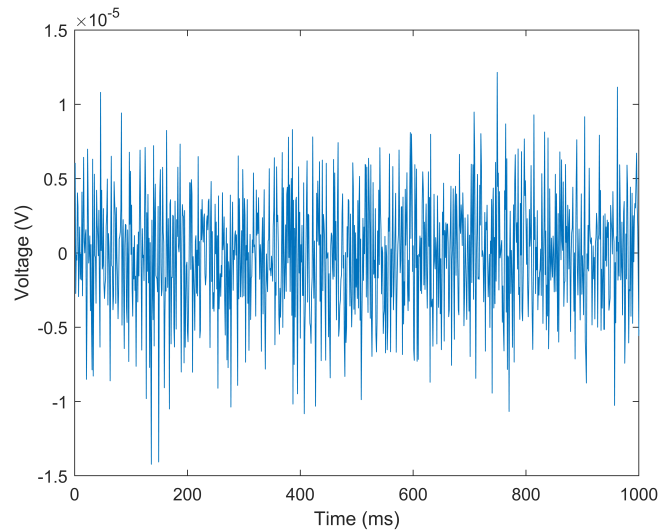
Figure 3.11: Output voltage calculated by summing the current noise sources and multiplying with the gain resistor of $1M\Omega$

It is desirable to have a diode that allows an increase in current flow for an increase in light irradiation without giving rise to other noise elements in the circuit. The output voltage is found from:

$$V_{no} = R_f \cdot (i_{nd} + i_{na} + i_{nr}) + v_{na} \tag{3.11}$$

For a higher value of R_f the noise at the output is also amplified. The combined effect of previously discussed noise sources can be seen in figure 3.11. This graph shows the noisy output voltage V_{no} which includes, the estimated shot noise, thermal noise and opamp current noise. The value for R_f used is $1M\Omega$. The mean of the output voltage is $0V$ with a standard deviation of $71\mu V$.

3.5.5 Inter-pyramid Distance and Noise

The distance between two pyramids 'd', as shown in figure 3.4, should be large enough for the pyramids to be able to sense two unique β values. However, when this condition is not satisfied, for either of the two pyramids, the error may be significant enough to overlap with the angular measurement from the other pyramid. Sources such as shot noise and thermal noise, assumed to be white noises with gaussian distribution, cause an error in measurement which is translated into an effective error in angular and proximity sensing. The total noise voltage frequency distribution is illustrated in figure 3.12, this is generated by plotting equation 3.11 in frequency domain.
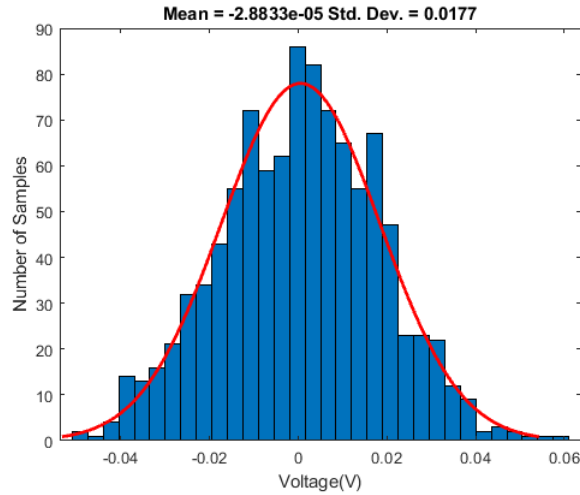
Figure 3.12: Estimated noise distribution as measured at the output of the opamp. The measured values of mean and standard deviation for the data set are also recorded.

The noise distribution is added to the input signal when calculating angular estimation β. The test angle used for this measurement is $75°$, at 100 and 1000 lumens of light brightness. This results in a distribution of samples around a mean of $75°$. This is illustrated in figure 3.13a and figure 3.13b. The distribution has a lower standard deviation in figure 3.13b because the light source is brighter than the light used in figure 3.13a.
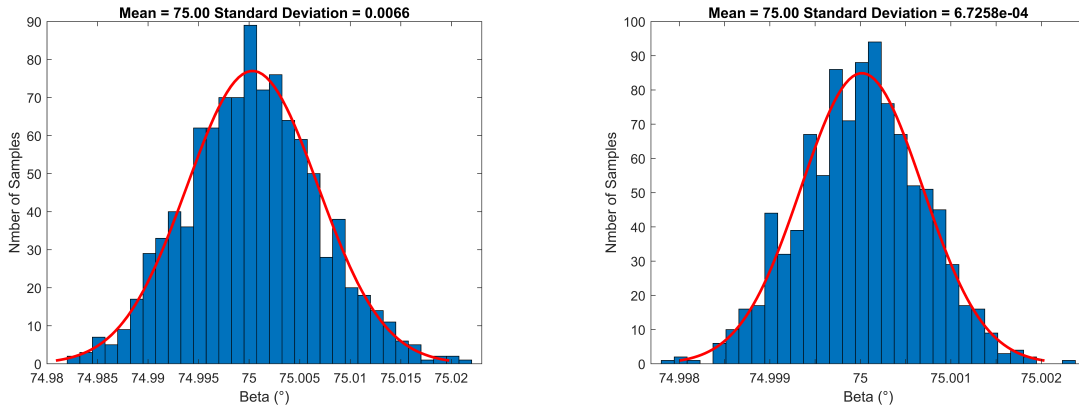
(a) The brightness of the light source is assumed to be 100 cd

(b) The brightness of the light source is assumed to be 1000 cd

Figure 3.13: Estimated noise distribution for a β of 75°

Figure 3.14 illustrates error in estimated β for a fixed 75° angle on incidence. The light intensity is varied from 50 to 225 lumens, and as expected, the error reduces with a brighter light source for a given fixed β.
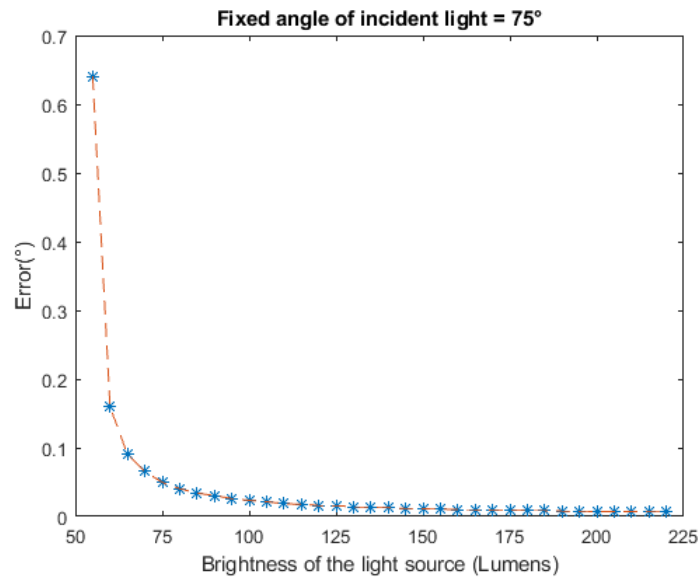
Figure 3.14: Error in estimated angle β for a light source with a fixed angle of incidence and varying light source intensity.

Figure 3.15 further illustrates the distribution of two angular measurements. The region of overlap as shown is the region of singularity for the proximity sensing system. When the, light source would be estimated to be at the point where the two parallel light sources converge or infinity.
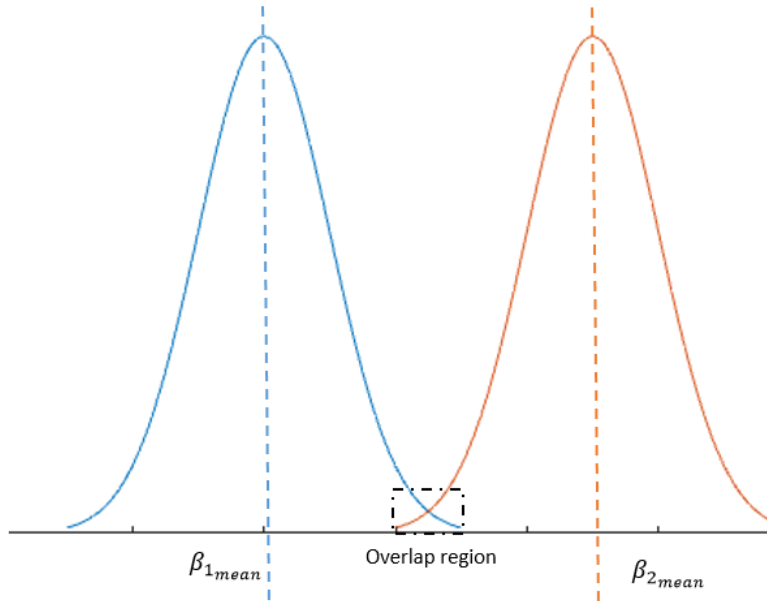
Figure 3.15: An overlap in two normally distributed curves where each curve represents the probability distribution for the measured angle from a single pyramid β. The overlap indicates a possibility of identical β values being recorded at a given time from two individual pyramids. $\beta_{1_{mean}}$ and $\beta_{2_{mean}}$ are the means for each β.

Higher the overlap area $P(\beta_1) \cap P(\beta_2)$, more are the possible values for which the two pyramids will measure the same β for a given instance in time. This overlap is inversely proportional to the inter-pyramid distance 'd', this is derived from equation 3.6. For a low error proximity sensing mechanism, the value β_{conv} is brought down by increasing inter-pyramid distance 'd' to a point until the overlap disappears. This simply means that the two pyramids are taken further away from each other so that it becomes less likely that they measure the same β.

Keeping the pyramids far way from each other will result in smaller errors in measurement. However, single chip integration of sensors limit the maximum practical separation between the sensors.

Chapter 4

Microfabricated Vector Light Sensor

This chapter discusses a micromachined model of vector light sensors. The 3D printed model we discussed in the previous chapter proves the concept needed to lay the foundation for creating a micromachined device with similar proximity sensing capability in a condensed form factor. This chapter also discusses the mask, package design, fabrication and characteristics of the new micro-scale sensor.

4.1 Fabrication

Micro-Fabrication is a process that enables fabricating micro and nano scale devices. High precision advanced instruments along with precise recipes are employed to create micro-scale devices. Since these devices are very small, the dust particles in air becomes comparable with the device's micro-structures. This is the reason the fabrication for these devices are carried out in a controlled and clean environment called a cleanroom. The fabrication process is carried out partly in Engineering Sciences cleanroom at Simon Fraser University and partly in 4D LABS. The cleanroom processes are performed by Vincent, a research engineer at Intelligent Sensing Lab.

The device that needs to be fabricated consists of multiple layers as shown in figure 4.1.

Figure 4.1: Micro-fabricated pyramid design

There are 5 major steps in the fabrication process using different masks to achieve pyramid structures with diodes on sidewalls, metal contacts to connect to these sidewalls, and finally

vias that connect to the P-type substrate. The fabrication process includes lithography, dopant implantation, etching, oxidation, and metal deposition. The steps for fabrication are briefly described as shown in figure 4.2.

The device has been fabricated on a P-type silicon wafer [78]. This is because the P-type substrate acts as the P-side or anode of the diode. A silicon dioxide layer was created on the wafer surface to pattern the pyramid opening. Wet oxidation [79, 80, 81] has been carried out in the oxidation furnace at the Engineering Science cleanroom at SFU. Oxidation is followed by photolithography to pattern the oxide and prepare the exposed region for etching[82, 83, 84, 85]. Etching in KOH solution consumes the oxide to create $54.7^{.}$ side wall angles. These inclined surfaces form the four sidewalls needed to form a pyramid. After etching, the wafer now has pyramid trenches needed for forming inclined PN junctions, this is possible because of the anisotropic nature of wet etching [86]. Through this process, the unneeded oxide was etched away and a new layer of oxide was grown for N-type doping [87]. The oxide mask was etched and dopants were implanted through openings on the wafer's surface. Next, the wafer was annealed for dopant implantation and repairing damages caused during etching. Next, openings for via contacts are created. These openings allow access to the underlying P-type substrate layer. Metallization [88] was carried out using liftoff technique [89]. Masks for each step are created using CoventorWare layout editor and are carefully aligned with the previous masks.

4.1.1 Thermal Oxidation

Thermal Oxidation is performed in the oxidation furnace. The silicon wafer is placed in a boat and pushed inside the oxidation chamber. The chamber is closed and an oxide layer grows on the silicon wafer's surface. This process also consumes the underlying silicon layer and a combination of this consumed silicon and the deposited oxide layer amount to the total thickness of the oxide layer.

4.1.2 Lithography

Lithography involves transferring the drawn patterns of geometric shapes in a mask to a thin layer of photoresist covering the wafer surface. Each mask used in the fabrication process is aligned with where the previous mask was, and then exposed to ultraviolet light. A photoresist consists of a photosensitive compound, resin, and an organic solvent. The photoresist used for this device is AZ-703 [90] which is a positive photoresist, this means that the UV exposed region of the photoresist layer becomes soluble and is then washed away with the AZ 300 MIF photoresist developer.
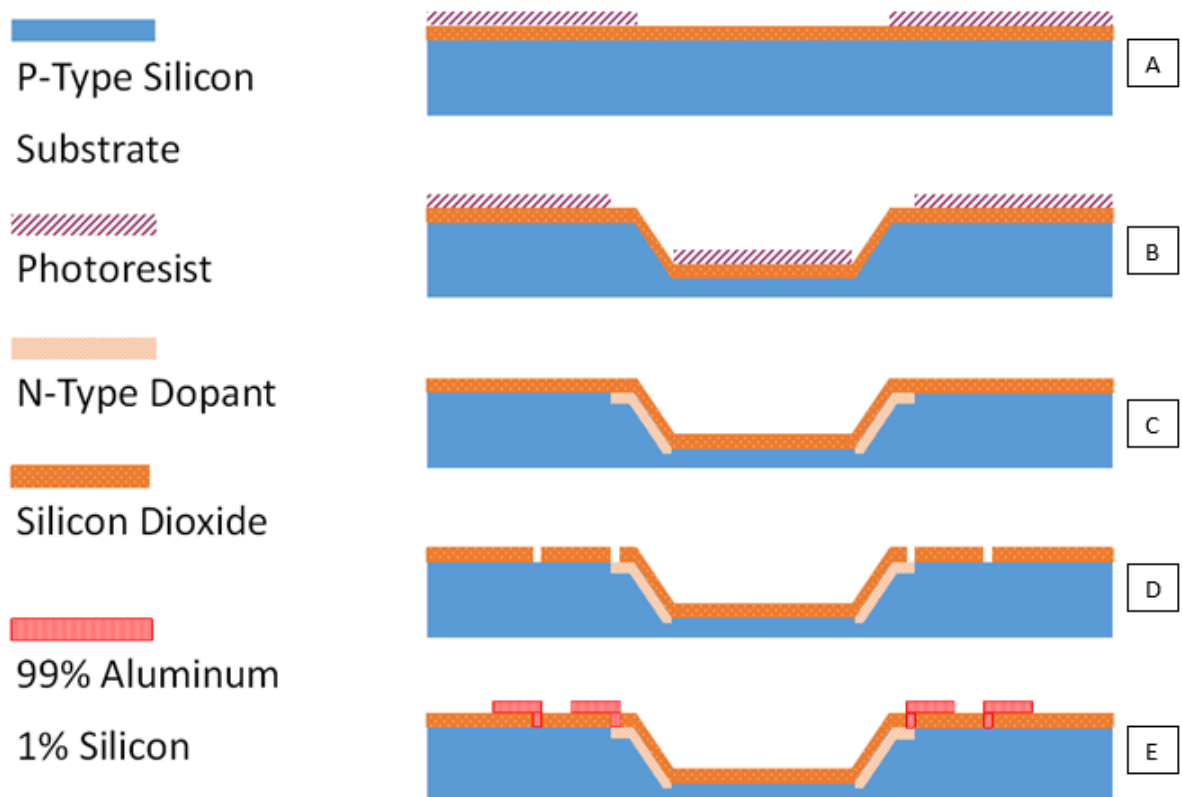
Figure 4.2: Steps for fabrication. A: Silicon Dioxide layer is grown and a photoresist is deposited; B: Post etching another silicon layer is grown and new photo lithography mask is deposited; C: N-Type Dopant is implanted followed by Oxide growth; D:Vias are formed; E: Metal is deposited through the vias

4.1.3   Etching

Etching is used to remove the unneeded silicon dioxide off the wafer surface. For the fabrication process a wet etching process is employed, which is performed by dipping the wafer into a Potassium Hydroxide (KOH) solution which dissolves the soluble and exposed silicon dioxide layer. The selectivity of KOH is high, which means the selected layer is removed entirely without harming the substrate and mask. KOH is an anisotropic etchant which makes it sensitive to the crystal orientation [91]. KOH displays an etch rate selectivity approximately 400 times higher in <100> crystal directions than in <111> directions, which is why it is possible to get sidewalls by stopping the etchant in the <111> plane. The <111> planes are the inclined walls as shown in figure 4.3, which form the pyramid sidewalls.

4.2 Microfabricated Model and Design

4.2.1 Single Pyramid

Post-fabrication, an inverted pyramidal structure with doped sidewalls inclined at an angle α with respect to the surface is formed. The PN junction is formed by the P type base substrate and the N type doped regions marked as D_{West} and D_{East} as shown in figure 4.3. This structure alone can measure the angle of incident light with respect to the sensor's position on the chip surface.
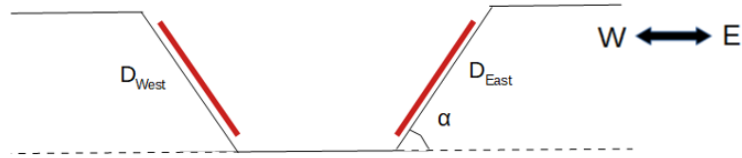
Figure 4.3: A single pyramid model schematic

4.2.2 Bi-pyramid

Extending the concept of using a single pyramid for angular estimation, it is also possible to have two such pyramid structures aligned in the same plane with photodiodes D_{South1} facing D_{North2} as shown in the figure.
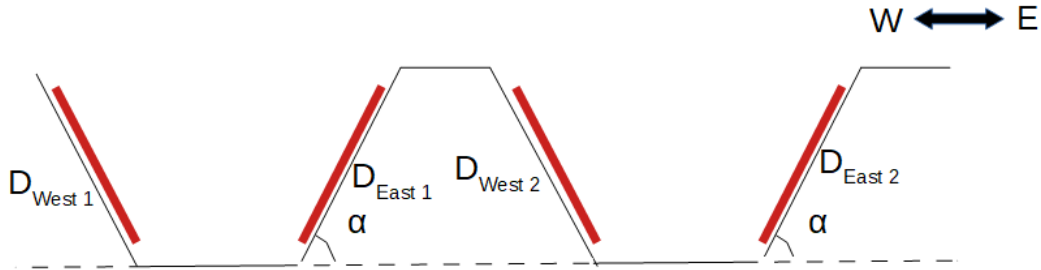
Figure 4.4: A 2 pyramid model schematic

Two such pyramids can be used to find two angles to a distant point in the same plane. Range detection in optical sensing becomes challenging when the pyramids are smaller and relatively closer to each other. The resolution of angle measurement can be increased by reducing the noise and increasing the input opamp's gain. For a lower gain, the noise is high but the dynamic range of proximity detection increases, for a higher gain the opamp saturates quickly and the dynamic range is limited to a few centimeters of range. There are a few challenges that appear while adjusting the gain of the opamp in real time applications.

4.3 Mask Design

This section discusses the mask design for fabricating a micro scale pyramid array. Because making multiple such pyramids would make a bulky device, the new version of sensors was made in a micro fabricated model with multiple pyramids placed at an equal distance from each other. The approach is to design a single pyramid with symmetric sidewalls. Anisotropic etching with KOH is used to achieve V-etched sidewalls that are inclined to the surface at a 54.7° angle.

A single pyramid with two sidewalls is used to extract angular information of the incident light on the pyramid's surface. It becomes interesting when there are multiple such light-detecting pyramids placed in a single row. The device needs 4 masks for fabrication, namely, Pyramid Mask, Doping Mask, Vias Mask, Metal Mask. The masks are drawn on CoventorWare [92], a Microelectromechanical systems (MEMS) design and simulation software. A single pyramid structure generated in CoventorWare is shown in figure 4.5.
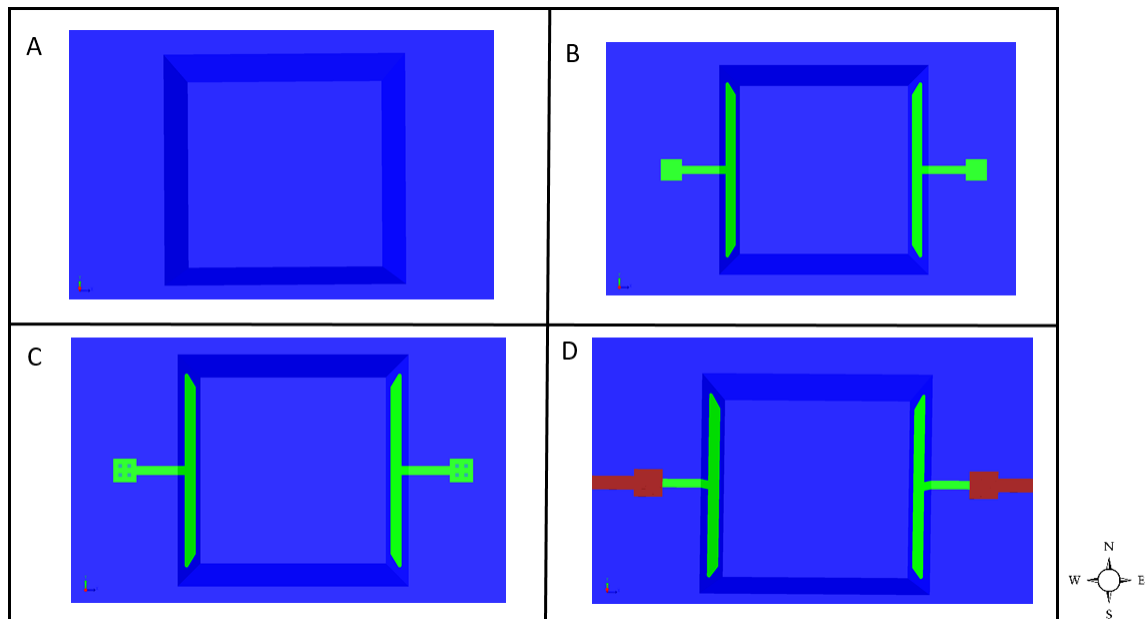
Figure 4.5: Mask design for a pyramid structure with two diodes doped on opposite facing facets. A: Mask to create the pyramid sidewalls B: After doping C: After adding vias D: After metallization

Mask A is the pyramid mask layer. This mask is used in creating the upper square structure on the wafer which is etched out using diluted KOH solution. This results in V-shaped sidewalls that form the 4 edges of the pyramid. Mask B is the doping mask, it shows two diodes that are formed by doping two opposite sidewalls of the pyramid. Mask C is the Via

mask, which creates an opening for contact vias. The tiny blue squares are vias - used to establish a path to connect to the P layer. Mask D is the metal mask which is used for electrical connection to the device.

A similar process is created for multiple pyramids. The idea is to use an established process and test the diodes and then form multiple pyramids on a single chip. Multiple combinations of pyramid structures were tested before developing the final sensor. The fabrication yield was about 70%.

Multiple pyramids are aligned in a row to form an array, this is illustrated in figure 4.6. This design is advantageous in the following ways:

1. Pyramids in the same plane can be used for height as well as angular measurements

2. Having multiple pyramids gives the flexibility of choosing pyramids at different distances from the first one which helps in choosing the best fit in terms of resolution for the desired application

3. The metal pads are at a distance from the actual sensing element, because wire bonds to the metal pads can cause unwanted reflections.
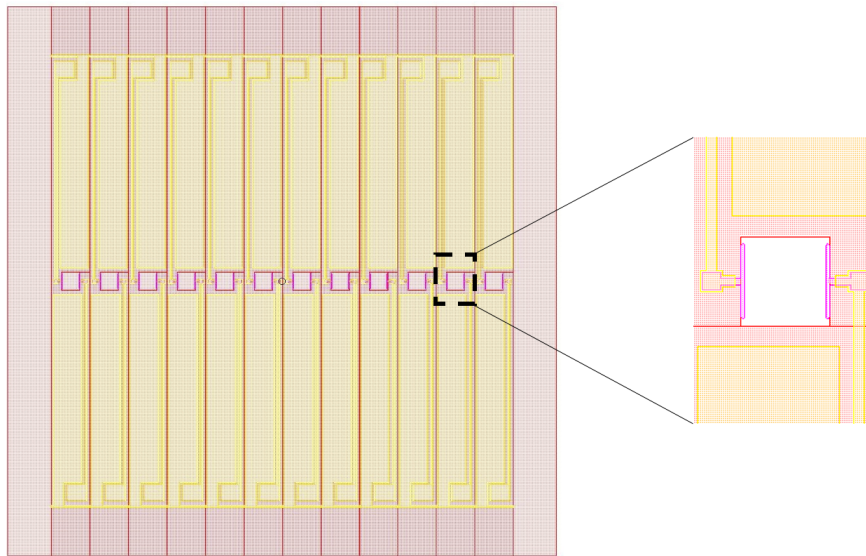
Figure 4.6: A design of the micro fabricated sensor which consists of a pyramid array arranged in a row structure. The vertical center of the design shows the pyramids and the upper and lower half of the rest of the chip shows metal contacts for each diode.

Having a row device is useful in cases where multiple reference points are needed for measurements in gesture recognition and motion sensing related application. Another added

advantage of the row structure is that the design allows a flexible testing regime. For instance, if one of the diode stops working, then a diode with similar orientation on the same surface can be used to replace the faulty diode. However, this would require recalculating the center of the new pyramid and then accounting for this offset in the proximity sensing formula.

Package

It is desirable that the sensor have a uniform and repeatable behavior, irrespective of the source beam size or intensity. A pin hole mask structure can be formed by punching a hole in an opaque sheet and placing this sheet above the sensor, such that, the light is able to illuminate at least two of the pyramids by the light filtered through the pin hole. The pyramid area may have have undesired doped regions around it. This means that the conductivity in certain surrounding region may change based on the light intensity. This is not a desirable phenomenon for the sensor's operation. This causes a fixed or variable bias to the output voltage. A pinhole structure blocks out the reflected interference light shining on the sensor, and channels the light directly to the inclined sidewall diodes that are needed for angular and height estimations by the sensor. The blocking mask needs to be opaque in nature so that no light passes through to the sensor. Figure 4.7 shows a mask and light sources of two different beam diameters.

(a) Small Light Source   *(b) Large Light Source*
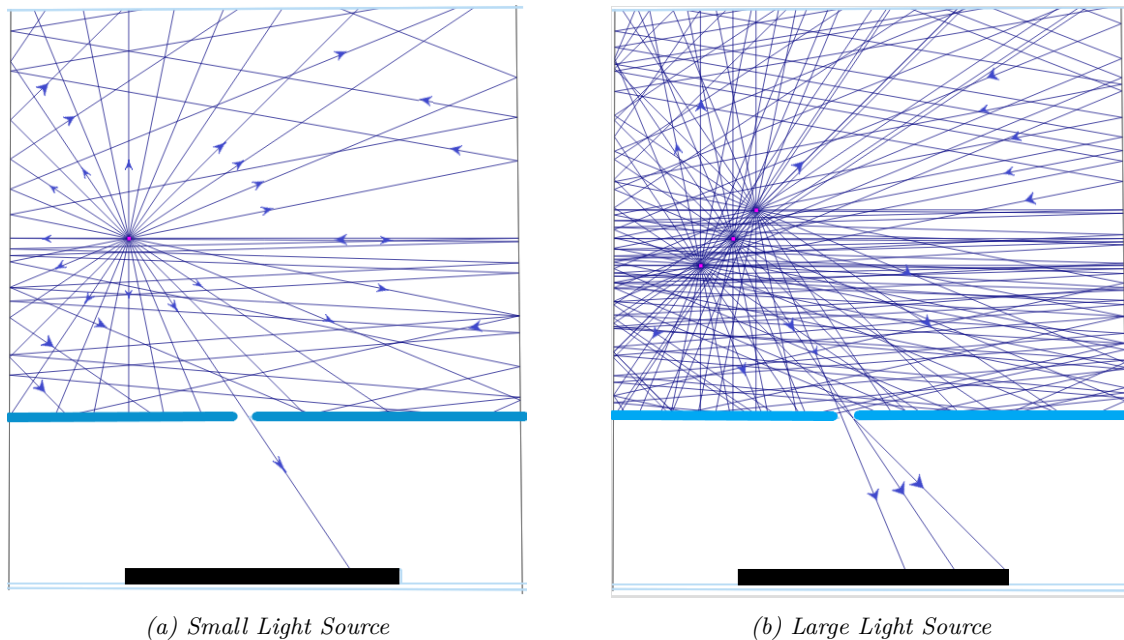
Figure 4.7: A pinhole mask fitted over a target sensor package. The two images show one and multiple omnidirectional light sources in the environment. The mask also blocks reflections which may otherwise impact the sensor's reliability.

For tests with multiple point light sources or a large light source relative to the sensor allows extra illumination on undesired photo active region. This can cause measurement errors as the light intensity on these regions become dominant. Figure 4.7 illustrates a light source in the environment the incident light of which illuminates the pyramid array. The pinhole only allows a certain amount of light to pass through, hence, mitigating the parasaitc's effect on the intensity measurements.

4.4   Characterization

Diode Characteristics
In this section the fabricated diode characterization is discussed. The ideal diode equation is:

$$I_d = I_0 \cdot \left(e^{\frac{qV}{nK_bT}} - 1 \right) + I_p \tag{4.1}$$

Measured IV characteristic for one of the fabricated photodiodes is illustrated in figure 4.8. The current recorded for each applied voltage value across the diode are shown.
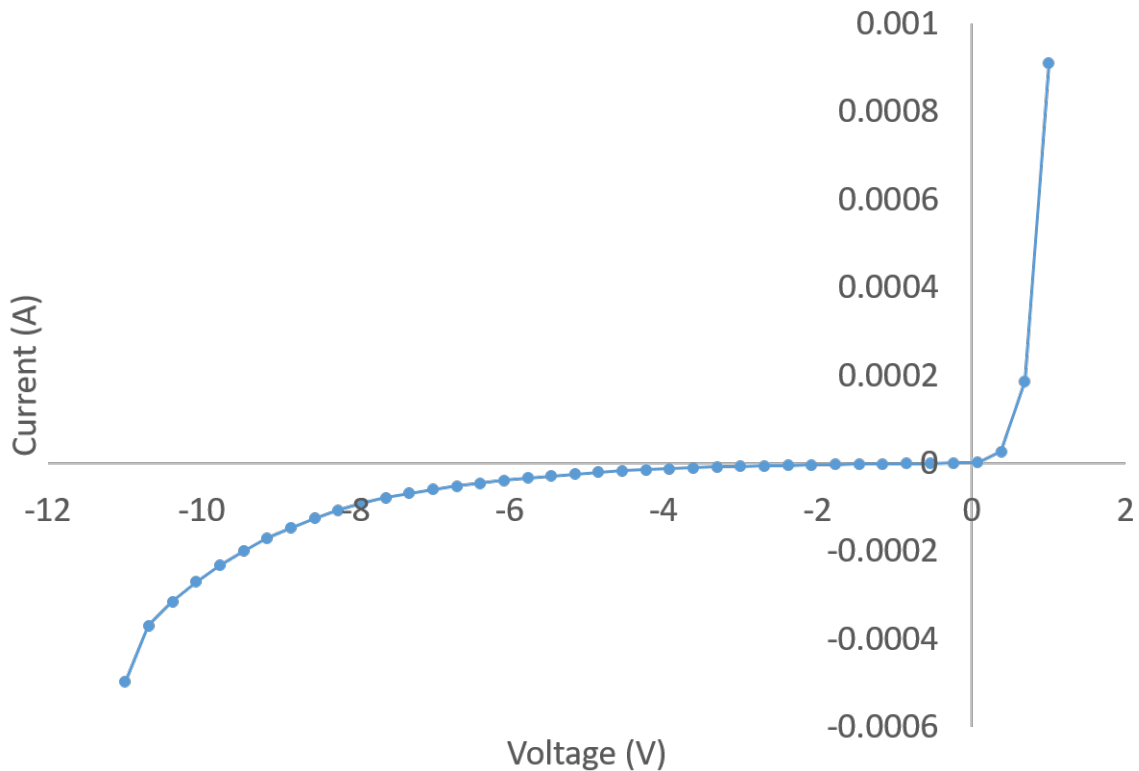
Figure 4.8: IV characteristics of fabricated photo-diode

The IVs are plotted using a data acquisition source measurement system. Source is limited to $5mA$ of maximum current and the voltage limit is set from $-11V$ to $+1V$. This is because the the diode characteristics show the breakdown and the knee in voltage in this range. The

diode is expected to forward bias at a $+0.7V$ potential difference across the diode junction. As figure 4.8 illustrates, there is almost no current flowing through the diode in reverse biased region and the diode starts conducting at a forward bias voltage of approximately 0.8V. However, when the reverse voltage across the diode is increased and it almost reaches breakdown - current starts flowing in the opposite direction as seen in figure 4.8.
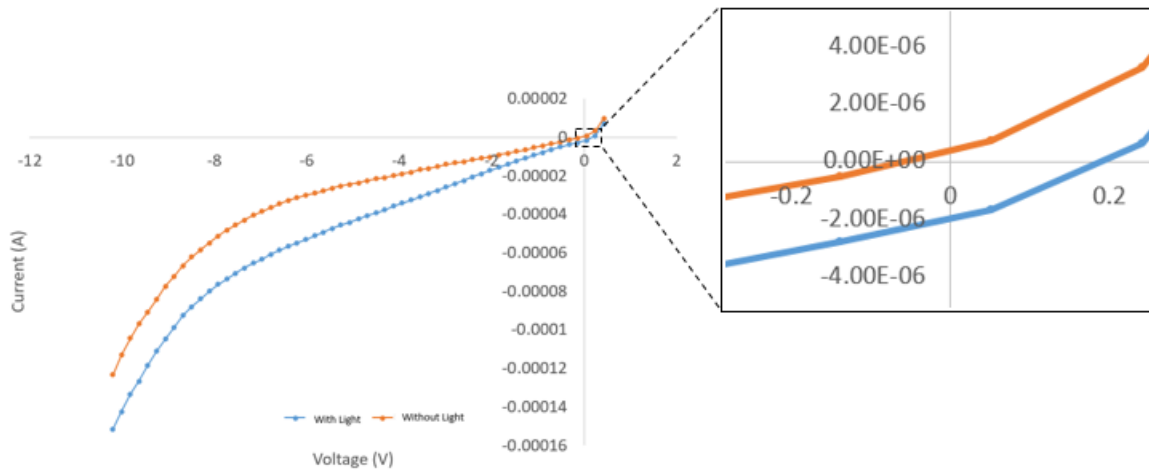
Figure 4.9: IV characteristics measured across a single diode in 'with light' and 'without light' conditions

Figure 4.9 shows how the current flow for a measured sample diode changes when there is light falling on the diode. For the entire reverse bias region as show there is a significant increase in the current flow.

Chapter 5

Experimental Results

This chapter discusses the practical and experimental implementation of the device designs and models. The experimental parameters are set in line with the simulation parameters. Further, the discussion carries on to interpretation of data, experimental setup, challenges faced while testing, device and design characterization, angular resolution, effects due to noise and the sensor's performance in angular and height detection.

5.1 Measurement Setup

This section discusses the sensing mechanism setup, the electronics used to obtain the data
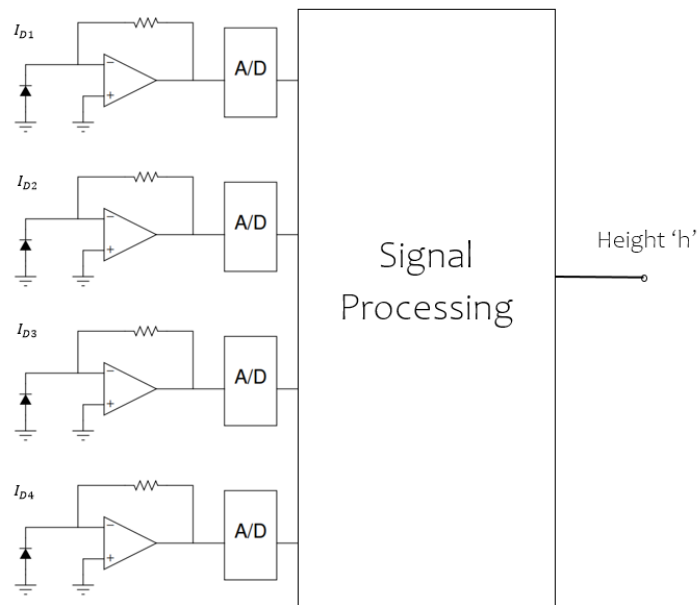
Figure 5.1: Data acquisition system for four source inputs I_{D1}, I_{D2}, I_{D3}, I_{D4} that are currents coming from independent photodiodes. The opamp amplifies and converts the current to an analog output voltage. The A/D gives a digital output to allow signal processing on the signal.

and the software interface used to troubleshoot the sensor. The packaged microfabricated sensor and the data acquisition controls are also briefly discussed.

Figure 5.1 shows a block diagram with four inputs which come from four independent diodes that are fixed to the pyramid sidewalls. The diode's cathode is connected to inverting input of the op-amp and anode is connected to ground. This zero biases the diode, which means that ideally no current should flow through the diode under no light or dark conditions.

For reverse biased diode with no light irradiated on it, the current flow is minimal and the output voltage is close to 0 Volts. Increasing the light source intensity would increase the photo-current I_p flowing through the diode. This current is flowing towards ground and can be indicated by negative Y direction shift of the IV's reverse bias characteristics, as shown in the IV curve in figure 4.8. Depending on the magnitude of this generated photo-current, the op-amp output also changes. Since the input of the diode is connected to the inverting input of the op-amp, the shift in voltage for a negative shift in current would be positive.
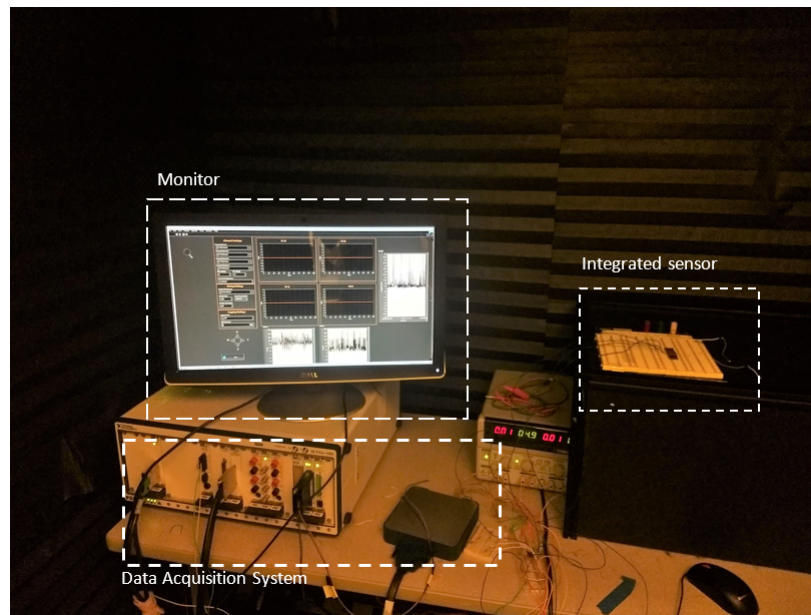
Figure 5.2: Experimental setup that shows a microfabricated sensor being used for proximity sensing inside a dark room

Figure 5.2 shows an experimental setup that consists of a computer with LabVIEW installed on it, an NI chassis which is placed below the monitor, a data acquisition system which is an extension of the NI data acquisition system, a dual DC power supply that powers the op-amp at $\pm 5V$, the microfabricated sensor which is packaged and connected to the breadboard which can be seen towards the extreme right of the setup. These components can be related to the block diagram that was discussed in figure 5.1. This will give an un-

derstanding of the electrical connections between the components.

To allow parallel data logging through the data acquisition system and real time processing of the logged data, a control interface is created in LabVIEW. This interface structure is illustrated in figure 5.3.
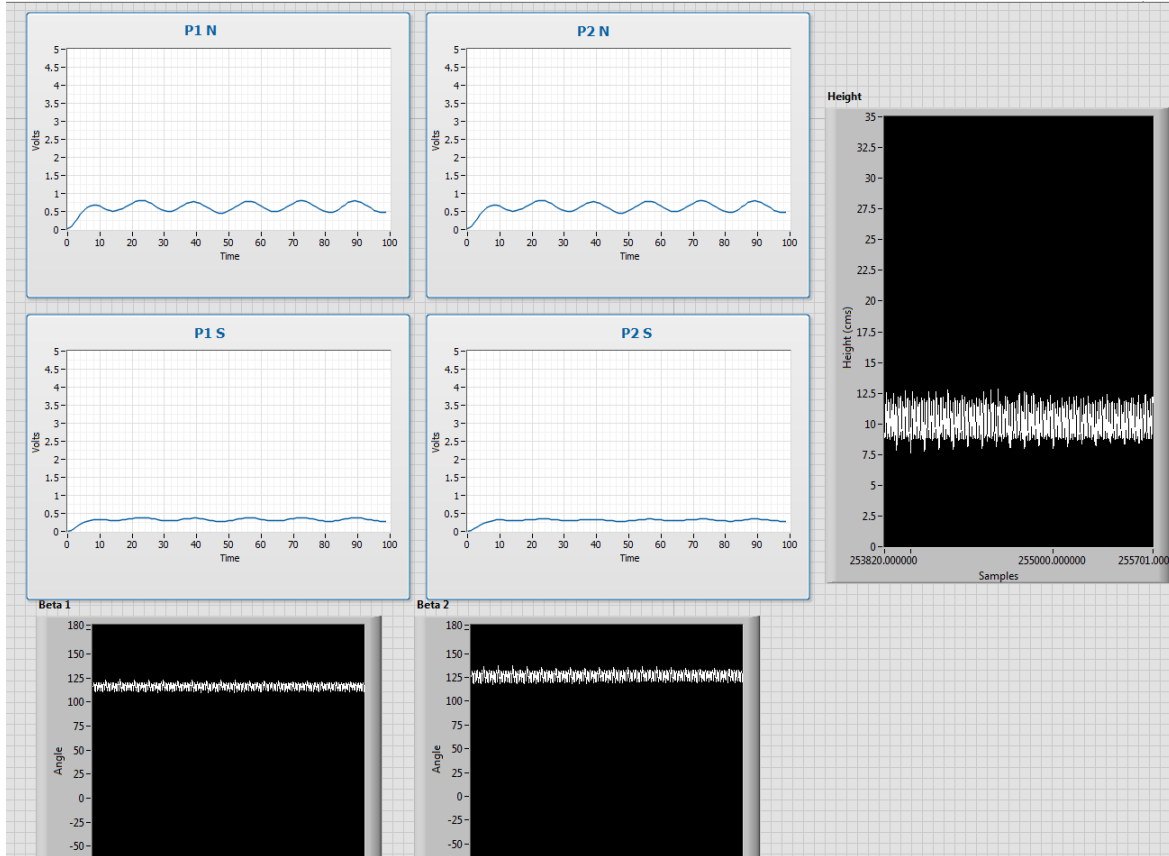
Figure 5.3: LabVIEW setup for real time angular and height measurements. $P1N$, $P2N$, $P1S$, and $P2S$ are voltage outputs from each diode, $Beta1$ and $Beta2$ plot the angular estimate of the light source, and $Height$ uses the Beta values to estimate proximity to the light source from the sensor.

Through the interface system, it is possible to individually monitor output voltage as measured from each diode on the sensor. This can be seen in the plots '$P1N$', '$P2N$', '$P1S$', and '$P2S$' in figure 5.3. '$Beta1$' and '$Beta2$' show the real time estimate of the measured angles β_1 and β_2. Using these angles, a LabVIEW code calculates the height and displays it as seen in '$height$'. This system provides a seamless interface with the NI chassis that connects NI data acquisition module with the sensor interface.

5.2 Measurement Results and Discussions

This section discusses two pyramid model designs that are used in angular and proximity sensing. Test results for both, the discrete photodiode model and microfabricated model

are discussed. The advantage of miniaturizing the model is that multiple proximity sensors can be put on the same chip while requiring the same amount of space that a 3D printed discrete photodiode model with one would need. A device with multiple such pyramid pixels would be able to extract more data from different points on the surface and can be used for applications such as gesture recognition, and motion sensing.

5.2.1   3D printed Pyramid

3D printed pyramid structures have been fabricated in SFU Surrey's workshop facility. The printed pyramids have two drilled holes on each facet and a rectangular slot created to accurately place the photodiodes on the pyramid sidewall. It is convenient to test the mathematical model on devices that can be physically adjusted or replaced in case of a fault. This work discusses a physical diode based model which uses multiple light sensors to ascertain light field information based on the incident light. The light source used in these experiments is a battery operated ~200 lumen white flash light.
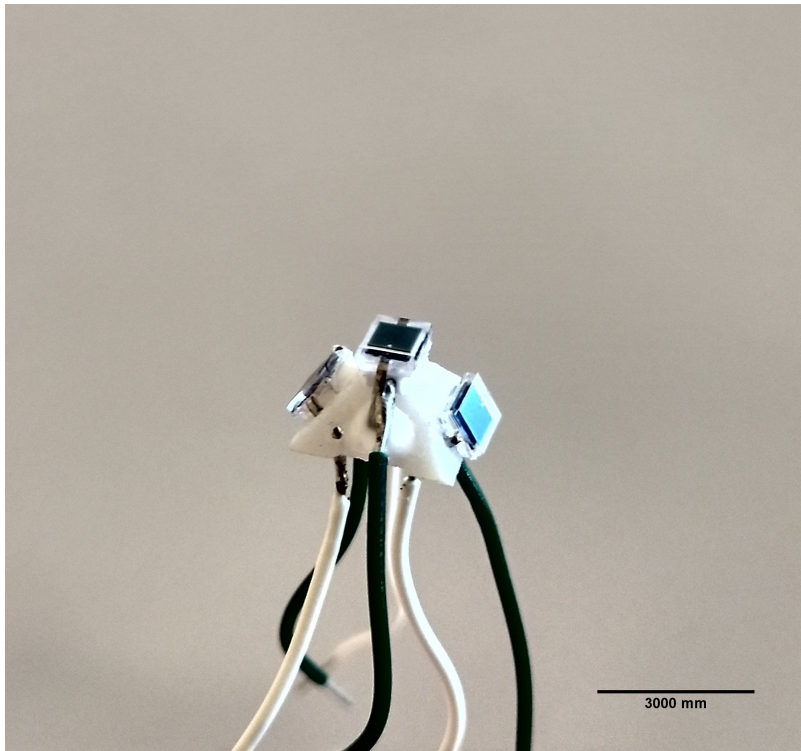
Figure 5.4: 3D printed proximity sensor used for angular and height measurements. This model uses a single pyramid to capture light field information.

Measurements with a 3D Printed Proximity Sensor

The pyramidal structure allows to have five surfaces, four sidewalls and a flat surface on the top that can be used for PN junction formations. Two opposite photodiodes in the same

40

plane can be used for angular estimation to the source. For height or proximity sensing, the same structure with a common diode on the flat top surface is used for measurements. To test the operating principle, a 3D printed pyramid model was designed. Figure 5.4 illustrates a test pyramid structure.

The model has 2 identical and symmetric holes drilled on each face of the pyramid. The photodiode leads are fitted in through these holes. Each face also has an extruded rectangular slot that matches the dimensions of the BPW34 photodiode. The photodiodes are press-fitted in the slot.

Angular Measurement

The test pyramid has been divided into two sub pyramids as previously discussed in section 3.4.2. One diode on the top acts as a common diode for the two virtual pyramids. The angles measured using the second pyramid (the one on the right) will be offset by $180°$ in reference to the first pyramid. The angular measurement for this setup is offset by $\pm 22.5°$ on each side because each virtual pyramid is tilted $22.5°$ above the surface. After taking theses numbers into account the test setup was built and angles estimations as perceived from each pyramid were recorded.
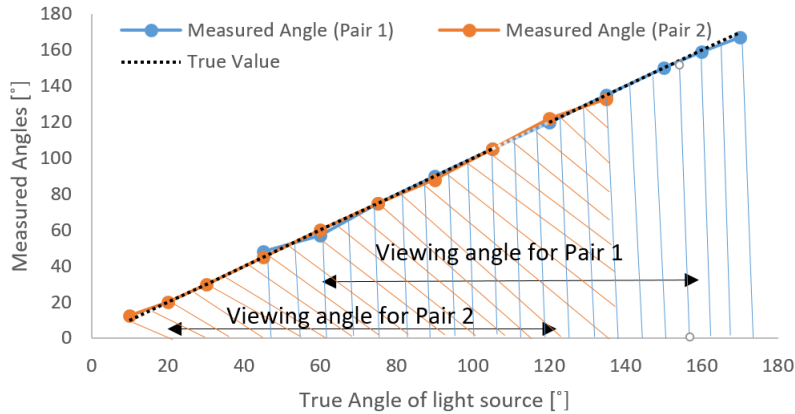
Figure 5.5: Angle measurements using 2 half pyramids. The photodiode on the top flat surface is shared between the the two sub pyramid pairs. One photodiode on each side along with the common photodiode contribute to a pyramid pair. The overlapping viewing angle for pair 1 and pair 2 define the range for which the measured angular and height values are reliable.

As illustrated in figure 5.5, the measured value from pair 1 and pair 2 overlap with the true value of incident light angle. For pair 1, the reliable viewing range is $45°$ to $157.5°$ and for pair 2 the viewing range is $22.5°$ to $135°$. Beyond these values the measurements are inaccurate and unreliable.

Height Measurement

Since a 3D printed model is tested for a light source very close to the sensor and a beam diameter comparable with the size of the pyramid, the sensor gets blinded for the first 2*cms* measured. This happens when all photodiodes on the pyramid are are not illuminated because the light source is that close to the sensor, and this is why values obtained in this range are discarded and not included in the test measurements. Figure 5.6 shows the height measurements recorded for every 2*cm* change in distance between the light source and the pyramid.
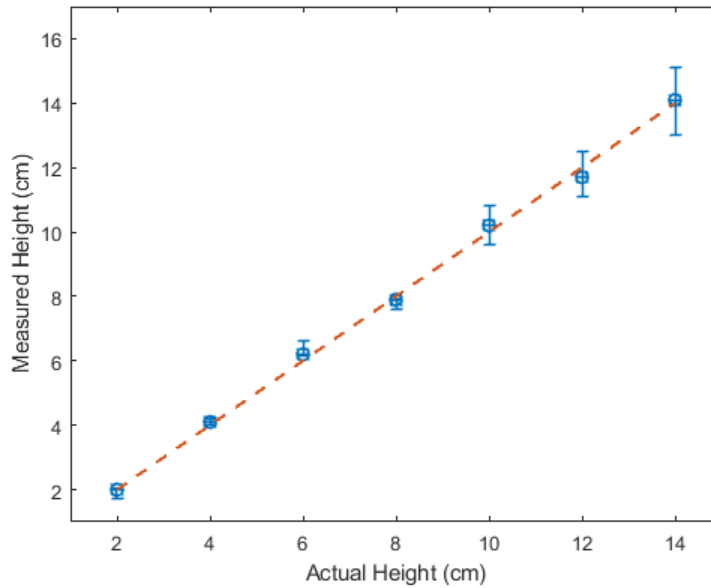
Figure 5.6: Height estimate from the 3 discrete diode pyramid structure

Since the pyramids are overlapping each other, the inter-pyramid distance '*d*' (as discussed in 3.4.1) is very small. For this reason, height estimations at higher distances become more challenging. Since the overlap in the probability distribution of the two β values is high, the chances of false overshoots in the measurements also increases.

Another factor that negatively impacts testing is the shared photodiode among the two pyramids. An offset in measurements from this specific photodiode would affect readings from both the pyramids. This also means that the pyramids would not be acting independently as in the case of the previously discussed bi-pyramid model.

5.2.2 Microfabricated Pyramid

This section, discusses test results when a microfabracated version of the sensors is used for measurements. The measurements provide angular and height estimations to the light source

from the sensor base. A model with one diode on each of the four facet of a pyramid has been discussed in [93]. This work proves that a pyramidal structure with light sensing side walls, can measure angular information of incident light. Figure 5.7a illustrates a pyramid with 4 photodiodes. This design shall be considered as the first generation device and the work presented in this document as the second generation device.

(a) Fabricated pyramid with four diodes

(b) Fabricated pyramid with two diodes
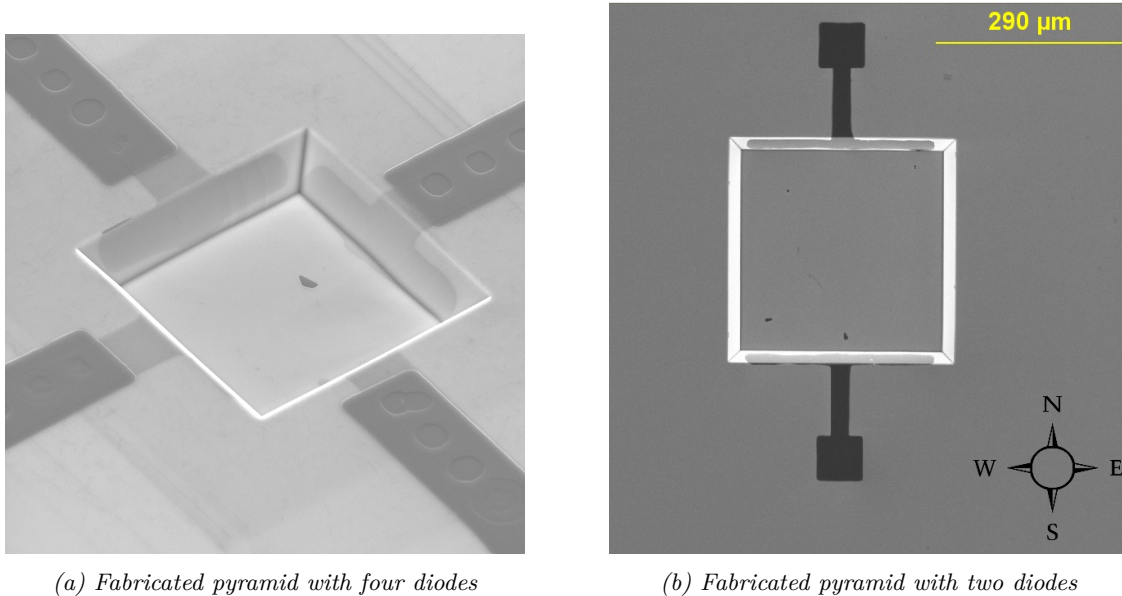
Figure 5.7: Pyramid structures used for testing

Microfabricated Row Array Pyramid

A pyramidal structure which is a part of the row array design is shown in figure 5.7. The mask design for the microfabricated row array pyramids has previously been discussed in section 4.3. The structure design is a micro-scaled version of the larger discrete 3D printed pyramid models. This design has been tested for angular and height measurements and the results are discussed in future sections of this document.

Angular Measurement

It is critical to have two diodes with similar IV responses that have similar sensitivity, dark current, and IV characteristics. Figure 5.7b shows a Scanning Electron Microscope (SEM) [94] image of an individual pyramid with two diodes fabricated on two opposite sides of the pyramid. In figure 5.7b, the square border are the 4 pyramid side walls formed by anisotropic etching of silicon. The two terminals coming out from two of the sidewalls are metal contacts to the doped N-region for each diode. The pyramid shown is symmetric and each diode is isolated from one another.

In-plane angular measurement is possible using a single pyramid with two opposite facing photodiode structures. For well structured diodes the incident light intensities should be the same if light is shining at a 90° angle with respect to the pyramid base. This also verifies the repeatability of the diode and the fact that an appropriate gain resistor has been used in the feedback for the transimpedance amplifier.

The light intensity measured on two opposite facing diodes should increase for one side when decreasing on the other and vice versa when the pair is reversed. Using the formula for β estimation as shown in 3.3, it is possible to find the angle measurement for the incident light on the device's surface. Figure 5.8 summarizes measured angular values for multiple captured data sets.
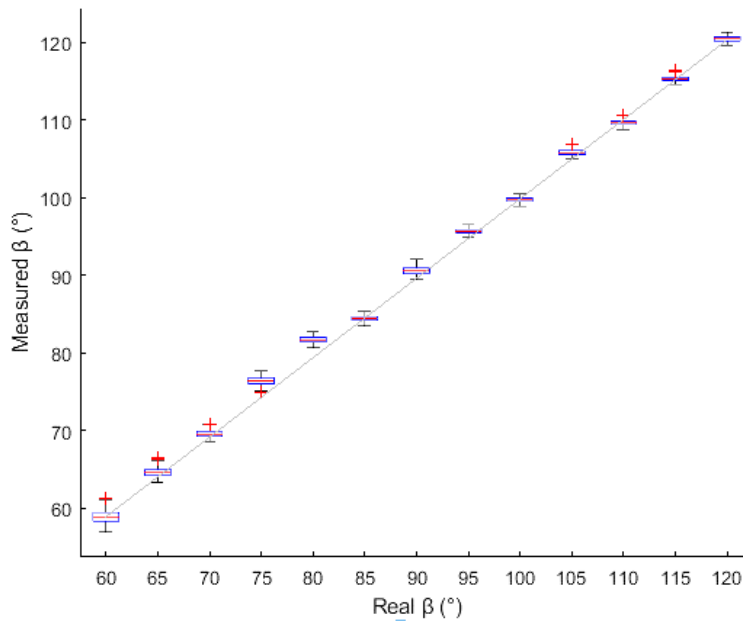
Figure 5.8: Angular measurement using one fabricated pyramid. The graph shows how the sensor's angular estimation fits with the actual (Real) incident angle of the light source.

The graph shows measured angles within the visibility range of the sensor which can be defined by angles where both sides of the pyramid are illuminated. Beyond this range, when one of the sides receive no light, the measurements are deemed unreliable and unpredictable. Based on figure 5.8, it is possible to conclude that angular measurements from a single pyramid are repeatable and reliable.

Real Time Angular Measurement

Figure 5.9 illustrates a real time measurement angular measurement using the microfabricated sensor. The upper half of the image figure 5.9 A, shows instantaneous voltage amplitude for the given sample time measured from 'Diode East' and 'Diode West'.
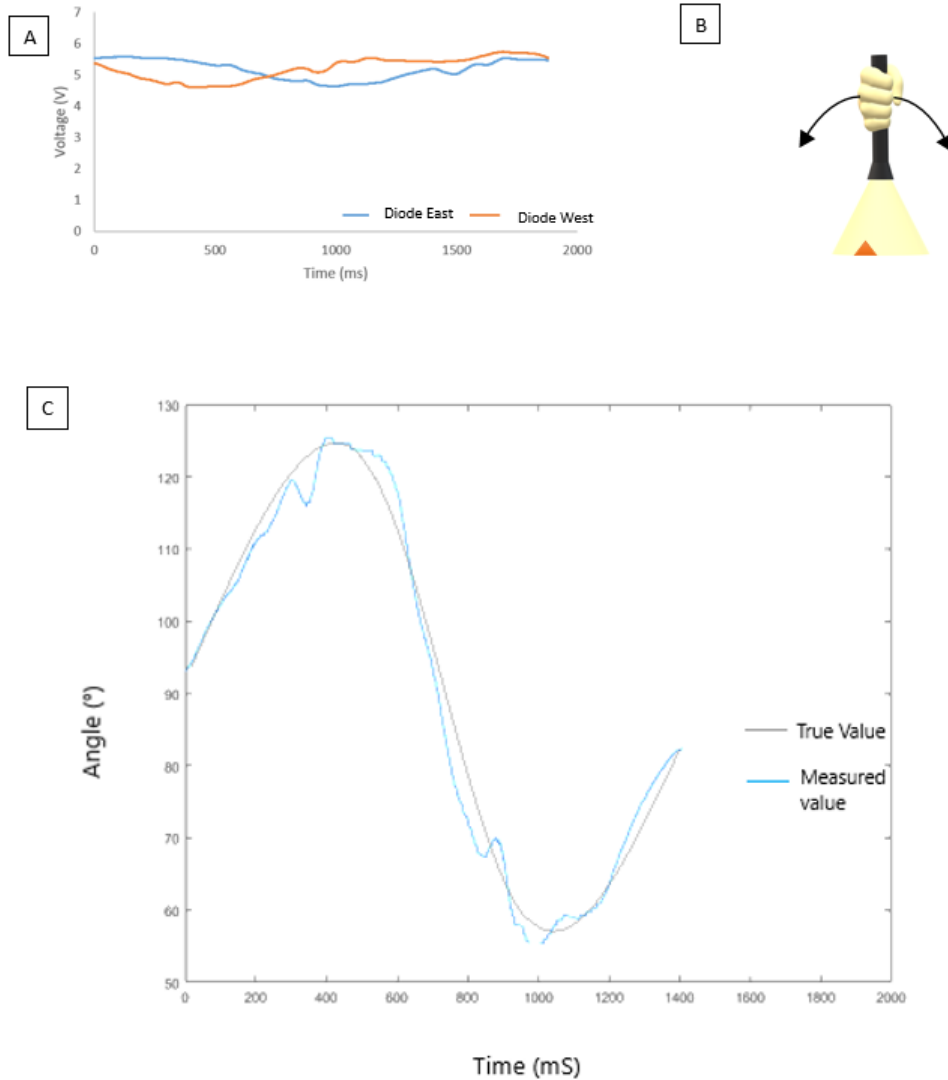
Figure 5.9: Real time angular measurements recorded using one pyramid on the fabricated sensor. A: Voltage measurements for the two diodes on the opposite sides of a pyramid. B: A light source held directly above a single pyramidal sensor model. C: Calculated angular measurement. β

When these values are plugged into the angle estimation formula 3.3, a real time angle plot of the incident light source angle can be plotted, this has been illustrated through figure 5.9 B.

The light source, a 250 lumen white light, was held in hand and moved from left to right

and back in the measuring axis of the photodiodes. This experiment verifies that the sensor can be used in a dynamic environment where the external factors affect the sensor's performance. The test is performed in an indoor environment with a bright light source incident directly over the test pyramid.

The estimated angles form a rough sinusoid which means that the angle changes have been fairly smooth and at a uniform pace, however some errors can be seen in the output because this device was hand held and the light was not necessarily following a constant plane.

Deviation in angle measurements based on source height

Experimentally, the error in measured β for a specific angle of incidence significantly increased as the light source was taken away from the sensor. This phenomenon was further investigated by testing the measured angle β by irradiating light at different distances from the sensor.
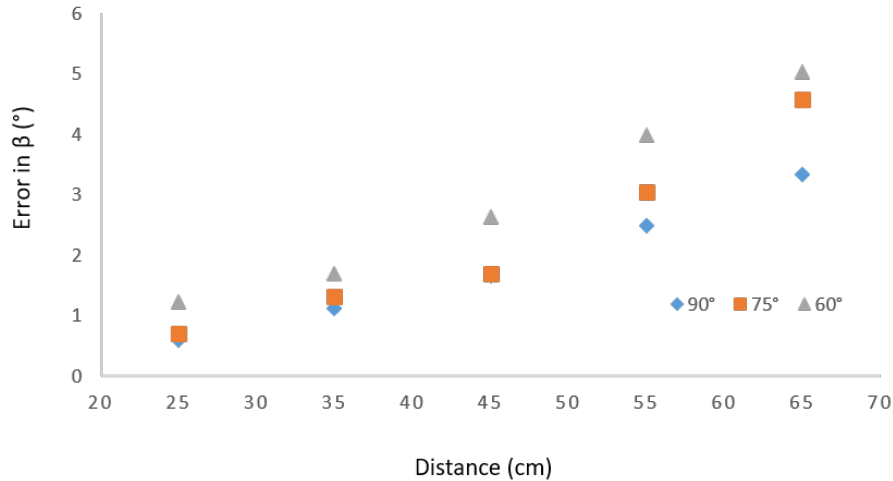
Figure 5.10: Standard Deviation measurements for varying light to sensor distances. Each point as indicated show the deviation in β from the original intended value, as the distance from the sensor increased

The test was carried out on 3 fixed angle of incidences, 60°, 75° and 90°. Figure 5.10 shows the results for angles 60°, 75° and 90° as the light source was moved away from the sensor. The Y-axis shows the standard deviation in measured β from the actual β. The

X-axis is the distance from the sensor to the light source.

The device symmetry allows us to assume similar results for 105° and 120° which is why we do not show this in the plot. For a 60° - angle of incidence, the light source is at the edge of the sensor's viewing angle. Here, the deviation range of β is the highest among all measured values as shown in the plot. This proves that the light when moving out of the field of view of the sensor becomes more prone to errors.

Light intensity – distance parameters follow an inverse square relation. The deviation from β increases when the light to sensor distance is increased. This is because the signal gets relatively weaker with distance and angle estimation gets more challenging.

Height Measurement

Multiple diodes on a chip are used for angular measurements which lead to light based distance sensing. More than two diodes are needed to achieve height estimation, all diodes have a slightly different IV curve and have some discrepancies in characteristics. It gets increasingly challenging to include reliable light intensity values from diodes as we keep increasing the number of diodes used for simultaneous measurements.
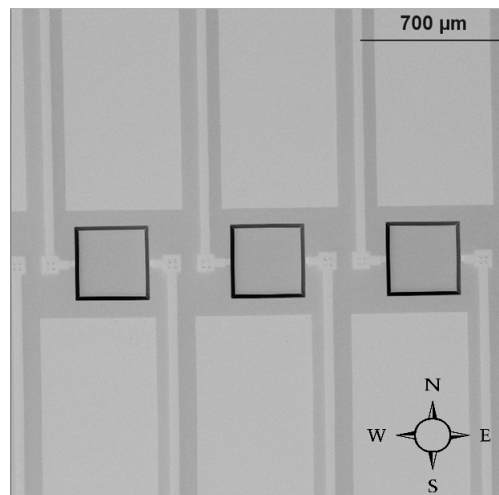
Figure 5.11: Fabricated 2-diode pyramids arranged in a row. The pyramids are arranged in line and the light is irradiated on the entire row. This structure helps determine angular positions from different points on the sensor's surface.

For height measurement, there is a need for a minimum of 3 diodes at different inclination angles or a combination of different inclination and physical position on the chip. Figure 5.11 shows an image of multiple pyramids placed next to each other in a row. These are pyramids similar to the ones shown in section 5.2.2.
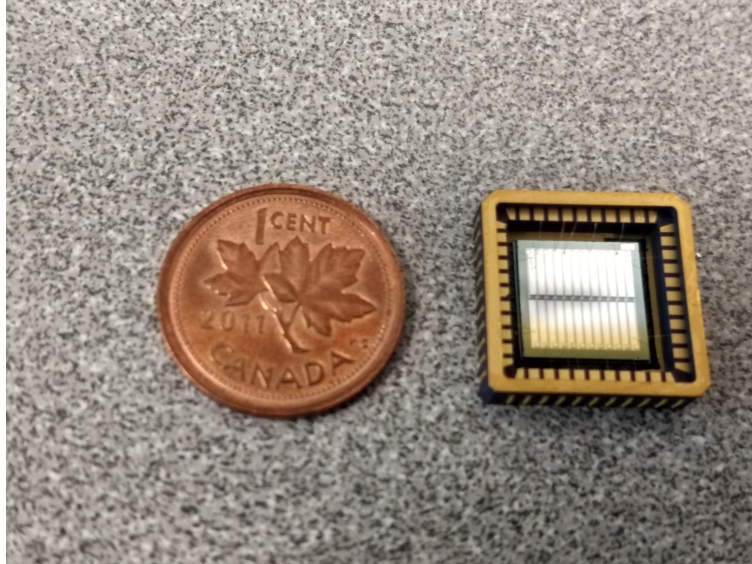
Figure 5.12: Fabricated and packaged sensor

The fabricated and packaged sensor is shown in figure 5.12. The sensor consists of 24 test diodes with wire bonds connecting the pads on the chip to the package's metal contacts.

The targeted sidewall doping has a minor undesired doped region which extends the diode's area on to the flat surface of the pyramids shown in figure 5.13. Light when incident on the chip illuminates the whole chip surface, this can cause a higher flow of current due to the unwanted flat PN junction formed by the extra doping beyond the sidewall. This can be resolved by better mask alignment while doping the sidewalls. Another way is to compensate for the extra amount of light absorbed by the diode.
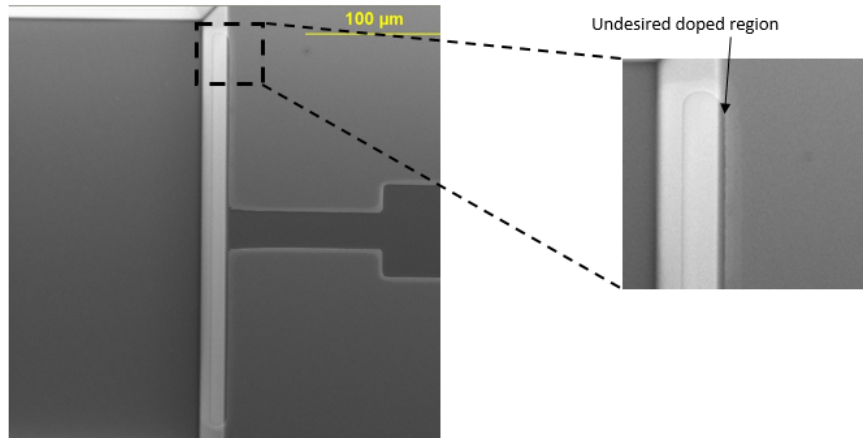
Figure 5.13: Undesired doped region extending the PN junction diode area for some of the diodes. The doping has been spread beyond the targeted sidewall region of the pyramid, on the flat surface.

Another problem faced while measurements was the absorption of heat by the silicon surface. The chip had some exposed silicon area which was used for routing paths from the metal pad to the pyramid sidewalls. However, with continuous usage, this surface tend to heat up and capture the stored energy. To solve this the unused region on the chip is covered with a metal layer which allows for better reflection of light and prohibits the chip from capturing heat. This further avoids reflection based crosstalk within the chip surface and allows only the intended diodes to receive the incident light.
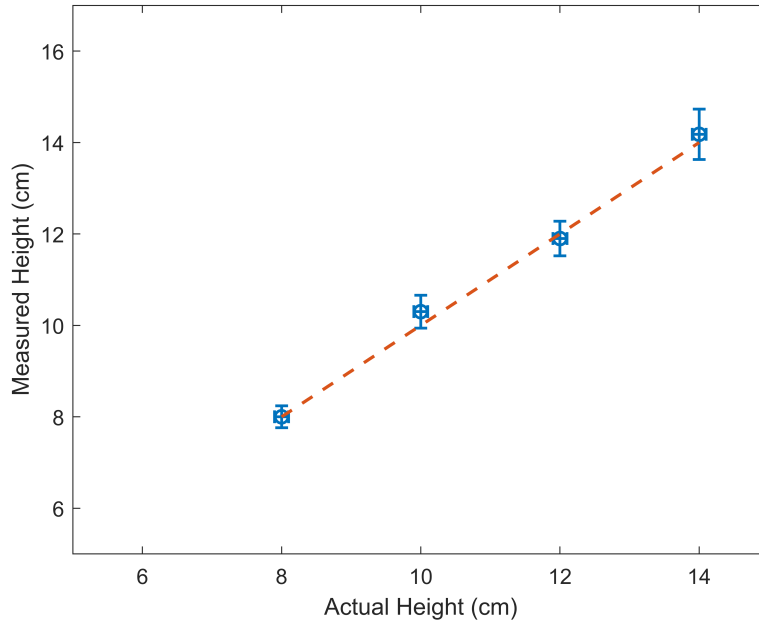
Figure 5.14: Height measurement using two pyramids $1500\mu m$ apart on a single microfabricated multiple pyramid sensor. Two inverted pyramids with photodiodes on opposite facets and in the same plane are used for these measurements.

Figure 5.14 summarizes the height measurements using an integrated model of row array pyramids. The distance between two pyramids is $1500\mu m$. The measured height is precise for shorter ranges of about $5cm$. to $15cm$., however, the uncertainty in predicting the correct height from the light source keeps increasing with the increase in height. The error bar is the standard deviation of the measurements. For distances too close to the sensor, the sensor perceives the light to be equally illuminating the pyramid facets and gives an uncertain output with a high amount of variation.

Figure 5.15 shows a similar summary of proximity data from a chip that has two pyramids at a $4000\mu m$ distance from each other. Because the two pyramids are more than twice the distance apart from each other, the height estimations improve significantly. This is because, the angular estimation error has reduced.
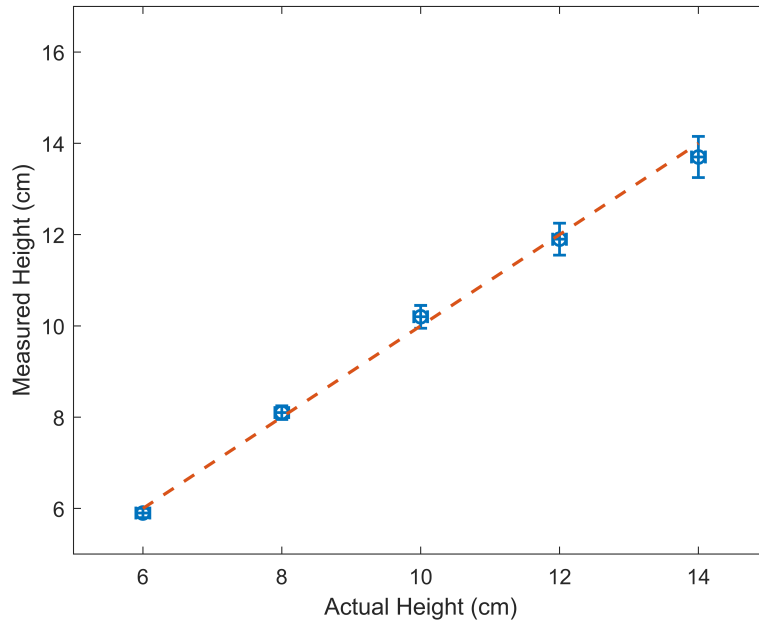
Figure 5.15: Height measurement using two pyramids $4000\mu m$ apart on a single microfabricated multiple pyramid sensor. Two inverted pyramids with photodiodes on opposite facets and in the same plane are used for these measurements.

In summary, the measurements are repeatable, the sensor is able to provide accurate proximity sensing. The performance of the sensor showed a significant improvement after allowing the light to pass through to only the pyramid region, leaving rest of the chip covered. This has made the readings more reliable and the device capable of being used in a dynamic and changing environment.

Chapter 6

Conclusion and Future Works

A proximity sensor measures the distance to an object within its field of view without establishing any physical contact with the target. Light based proximity sensing use the light's intensity to determine the vicinity to an object. Such proximity sensors are widely used in robotics, automatic industrial equipment and smart phones among many other applications throughout the industry. For many upcoming technologies, proximity sensors are becoming critical to the device's overall performance. Some factors such as the sensor's size, resolution and power usage are instrumental in deciding the appropriate sensor for a given application. The current trend of sensor fusion to improve device resolution requires integrating multiple proximity sensors in a package to further improve resolution in proximity sensing.

6.1   Summary

This work discusses proximity sensing using a pyramidal sensor pixel model. The device is passive in operation because it uses environmental light for proximity sensing. This sensor also uses low power because it does not operate on the principle of emitting waves into the environment. A prototype model showing a 3D printed structure with discrete diodes is used to prove the concept. This sensor is micro-fabricated, tested and packaged into a single chip. The microfabricated device has been used for determining angular and height measurement. The sensor and the data acquisition circuit are discussed. Sources of noise in the circuit and ambient light noise are talked about. A pin hole is used to reduce the sensor's response to parasatics. A LabVIEW interface is developed to test the device in real time. This interface provides individual views to monitor the light intensity measured by each diode and incorporates the formula to calculate angle and height to the incident light source. The device's accuracy and repeatability is more reliable for small distances, hence, this device can be used in applications that require short range detection. Because this device uses low power it can be connected to a portable robot and be used in short range navigation and proximity sensing. Automotives are using an array of sensors for proximity sensing and detection for both small and long range applications to provide a better driving

experience to the user. With upcoming automatic driver-less car technology, the reliance on such sensors would increase in the future. This sensor has a huge potential in many more industries that are working towards automating their technologies.

6.2   Contributions

The microfabricated sensor presented is a passive sensor that can find multiple applications in mobile devices. The sensor gives an alternative to proximity sensing devices that actively radiate waves. This is a low power, robust and economic device. The fact that the sensor can be scaled to a micro-level proves that the device can easily be embedded into robotic bodies, smartphones, and other equipment that use proximity sensing. This work has resulted in the following work:

- A. Rai, D. Zhuo, B. Bahreyni,"Passive Proximity Detection Based on a Miniaturized Pyramidal Optical Sensor", IEEE Sensors 2019, Montreal.

- D. Zhuo, A. Rai, S. Grayli, G. Leach, B. Bahreyni,"A Micromachined Vector Light Sensor", Journal paper.

6.3   Future Work

Irrespective of how much a device is tested and reformed, there is always scope for not only performance improvements but also for use in a variety of proximity sensing applications. The microfabricated device has a limited range and limited pyramid pixels on a single chip. This document provided a discussion on the model and subsequent tests to verify the model. The optical sensing mechanism using a pyramid pixel can be further explored by trying different structural geometries and possibly moving forward with a denser chip design. Some of the suggested possibilities of further improving such an optical sensor are:

Adaptive Resolution for Range Enhancement: The height calculations achieved are limited by the opamp saturation. For a high light intensity the sensor is blinded. This can be seen as similar to what a camera would act like if a bright light bulb is placed very close to the camera lens. The OpAmp can be used with a lower gain to improve the dynamic range but this negatively impacts the resolution of the data acquisition system and a lot of information gets rounded up due to quantization error when converted from analog to digital form. Using a reference pyramid with low gain can estimate the position of the light source with a low resolution. A secondary pyramid with a higher gain can now capture a higher resolution proximity estimation of the same light source based on the initial estimate by the low-gain sensor.

Sensor Fusion: Sensor fusion is the idea of using multiple sensors in tandem to improve a system's performance. For proximity sensing this can be implemented by using different kinds of proximity sensors to estimate distance to the same target. For example, using ultrasonic sensor would give more accurate results when sensing proximity to a glass object as compared to an infrared sensor. However, an infrared sensor per se is highly accurate and repeatable for sensing proximity to opaque targets. A combination of these sensors improves the device's performance and avoids relaying false information to the user. This light sensor can also be used in tandem with other similar proximity sensing devices. Since this sensor uses low power it can be used in devices that need offline sensing. Offline sensing is an idle state for the robot, when all other sensors are switched off or put into low power mode.

CMOS design: This design can be further fabricated with a CMOS fabrication technique. However, building a sensor on a smaller scale would require rework on the fabrication process, circuit design, and improvements in the device model. A highly dense chip can achieve better image resolution capabilities of a captured image and also allow for modification using advanced deep learning algorithms to correct pixel readouts based on neighbouring pixels.

Gesture recognition: It is already possible to sense a light source in space using this sensor design. With a denser chip design, it is possible to create an algorithm that can support gesture recognition techniques. Since this optical method of sensing uses passive means for proximity measurements, it uses low power and can be used in mobile devices for applications that need continuous gesture recognition embedded in their system.

Bibliography

[1] G. Benxing and G. Wang, "Underwater image recovery using structured light," *IEEE Access*, vol. 7, pp. 77183–77189, 2019.

[2] Y. V. Shulgina, A. A. Soldatov, E. M. Shulgin, and A. V. Kudryashova, "Acoustic borehole depth-gauge with the dual-frequency sensing method," in *2016 International Siberian Conference on Control and Communications (SIBCON)*, pp. 1–5, May 2016.

[3] S. Zhu, Y. Xu, D. Li, and Z. Wu, "A sample and hold time-to-amplitude converter for single photon time-of-flight measurement," in *2019 IEEE 9th Symposium on Computer Applications Industrial Electronics (ISCAIE)*, pp. 316–319, April 2019.

[4] A. Ficorella, L. Pancheri, F. Acerbi, and C. Piemonte, "Effect of cell size on ambient light rejection in sipm-based time-of-flight range sensors," in *2017 IEEE SENSORS*, pp. 1–3, Oct 2017.

[5] Y. Duan, L. Yan, Y. Zhong, and J. Yao, "A new method of improving height accuracy of airborne photogrammetry using a multi-camera system," in *2014 IEEE Geoscience and Remote Sensing Symposium*, pp. 2019–2022, July 2014.

[6] Z. Wang, Y. Liu, Q. Liao, H. Ye, M. Liu, and L. Wang, "Characterization of a rs-lidar for 3d perception," in *2018 IEEE 8th Annual International Conference on CYBER Technology in Automation, Control, and Intelligent Systems (CYBER)*, pp. 564–569, July 2018.

[7] K. Koyama, M. Shimojo, T. Senoo, and M. Ishikawa, "High-speed high-precision proximity sensor for detection of tilt, distance, and contact," *IEEE Robotics and Automation Letters*, vol. 3, pp. 3224–3231, Oct 2018.

[8] G. Thiel, "Automatic cctv surveillance-towards the virtual guard," *IEEE Aerospace and Electronic Systems Magazine*, vol. 15, pp. 3–9, July 2000.

[9] R. Behrendt, "Traffic monitoring radar for road map calculation," in *2016 17th International Radar Symposium (IRS)*, pp. 1–4, May 2016.

[10] Shuzhou Jiang, Hui Xue, A. Glover, M. Rutherford, and J. V. Hajnal, "A novel approach to accurate 3d high resolution and high snr fetal brain imaging," in *3rd IEEE International Symposium on Biomedical Imaging: Nano to Macro, 2006.*, pp. 662–665, April 2006.

[11] Z. Hu, T. Li, Y. Yang, X. Liu, H. Zheng, and D. Liang, "Super-resolution pet image reconstruction with sparse representation," in *2017 IEEE Nuclear Science Symposium and Medical Imaging Conference (NSS/MIC)*, pp. 1–3, Oct 2017.

[12] H. Irmak, G. B. Akar, and S. E. Y. uksel, "Image fusion for hyperspectral image super-resolution," in *2018 9th Workshop on Hyperspectral Image and Signal Processing: Evolution in Remote Sensing (WHISPERS)*, pp. 1–5, Sep. 2018.

[13] J. G. Cham, S. A. Bailey, J. E. Clark, R. J. Full, and M. R. Cutkosky, "Fast and robust: Hexapedal robots via shape deposition manufacturing," *The International Journal of Robotics Research*, vol. 21, no. 10-11, pp. 869–882, 2002.

[14] Paryanto, M. Brossog, M. Bornschlegl, and J. Franke, "Reducing the energy consumption of industrial robots in manufacturing systems," *The International Journal of Advanced Manufacturing Technology*, vol. 78, May 2015.

[15] S. Soloman, *Sensors Handbook (2nd Edition)*. McGraw-Hill Professional Publishing, 2009.

[16] Y. Yamada, K. Ookoudo, and Y. Komura, "Layout optimization of manufacturing cells and allocation optimization of transport robots in reconfigurable manufacturing systems using particle swarm optimization," in *Proceedings 2003 IEEE/RSJ International Conference on Intelligent Robots and Systems (IROS 2003) (Cat. No.03CH37453)*, vol. 2, pp. 2049–2054 vol.2, Oct 2003.

[17] A. P. Joy, M. Kanygin, and B. Bahreyni, "Measurement of mechanical strain based on piezo-avalanche effect," in *Applied Physics Letters*, vol. 114, 2019.

[18] T. Eamsa-ard, T. Seesaard, and T. Kerdcharoen, "Wearable sensor of humanoid robot-based textile chemical sensors for odor detection and tracking," in *2018 International Conference on Engineering, Applied Sciences, and Technology (ICEAST)*, pp. 1–4, July 2018.

[19] R. Woodman, A. F. Winfield, C. Harper, and M. Fraser, "Building safer robots: Safety driven control," *The International Journal of Robotics Research*, vol. 31, no. 13, pp. 1603–1626, 2012.

[20] Z. Gu, Q. Zeng, X. Xiao, and M. Huang, "Relay switching at zero-crossing point of grid voltage to eliminate the eft interference," in *2018 IEEE International Symposium on Electromagnetic Compatibility and 2018 IEEE Asia-Pacific Symposium on Electromagnetic Compatibility (EMC/APEMC)*, pp. 1248–1250, May 2018.

[21] J. H. Hines, "Review of recent passive wireless saw sensor and sensor-tag activity," in *2011 4th Annual Caneus Fly by Wireless Workshop*, pp. 1–2, June 2011.

[22] J. Haverinen, M. Parpala, and J. Roning, "A miniature mobile robot with a color stereo camera system for swarm robotics research," in *Proceedings of the 2005 IEEE International Conference on Robotics and Automation*, pp. 2483–2486, April 2005.

[23] N. Sakib, Z. Ahmed, A. Farayez, and M. H. Kabir, "An approach to build simplified semi-autonomous mars rover," in *2016 IEEE Region 10 Conference (TENCON)*, pp. 3502–3505, Nov 2016.

[24] F. Basso, E. Menegatti, and A. Pretto, "Robust intrinsic and extrinsic calibration of rgb-d cameras," *IEEE Transactions on Robotics*, vol. 34, pp. 1315–1332, Oct 2018.

[25] Su Yeong Jeong, Byoung Chul Kim, and Young Han Kim, "Defect detection in a cylinder using an ir thermographic device and point heating," in *2007 International Conference on Control, Automation and Systems*, pp. 2389–2392, Oct 2007.

[26] M. Y. Shieh, Y. H. Chen, J. H. Li, N. S. Pai, and J. S. Chiou, "Fast object detection for human-robot interaction control," in *Proceedings of the 2013 IEEE/SICE International Symposium on System Integration*, pp. 616–619, Dec 2013.

[27] D. Balek and R. Kelley, "Using gripper mounted infrared proximity sensors for robot feedback control," in *Proceedings. 1985 IEEE International Conference on Robotics and Automation*, vol. 2, pp. 282–287, March 1985.

[28] I. Anwar and S. Lee, "High performance stand-alone structured light 3d camera for smart manipulators," in *2017 14th International Conference on Ubiquitous Robots and Ambient Intelligence (URAI)*, pp. 192–195, June 2017.

[29] Y. Li, Q. L. Wang, Y. F. Li, De Xu, and M. Tan, "On-line visual measurement and inspection of weld bead using structured light," in *2008 IEEE Instrumentation and Measurement Technology Conference*, pp. 2038–2043, May 2008.

[30] Q. Wu, X. Wu, and F. Zhong, "Structural analysis of size of machine vision measuring system based on structured light and its experimental study," in *2011 Second International Conference on Digital Manufacturing Automation*, pp. 1121–1124, Aug 2011.

[31] L. Cruz, D. Lucio, and L. Velho, "Kinect and rgbd images: Challenges and applications," in *2012 25th SIBGRAPI Conference on Graphics, Patterns and Images Tutorials*, pp. 36–49, Aug 2012.

[32] M. A. Tehrani, A. Saghaeian, and O. R. Mohajerani, "A new approach to 3d modeling using structured light pattern," in *2008 3rd International Conference on Information and Communication Technologies: From Theory to Applications*, pp. 1–5, April 2008.

[33] J. Geng, "Structured-light 3d surface imaging: a tutorial," *Adv. Opt. Photon.*, vol. 3, pp. 128–160, Jun 2011.

[34] J. Noraky and V. Sze, "Low power depth estimation for time-of-flight imaging," in *2017 IEEE International Conference on Image Processing (ICIP)*, pp. 2114–2118, Sep. 2017.

[35] O. Arif, W. Daley, P. Vela, J. Teizer, and J. Stewart, "Visual tracking and segmentation using time-of-flight sensor," in *2010 IEEE International Conference on Image Processing*, pp. 2241–2244, Sep. 2010.

[36] R. Tanner, M. Studer, A. Zanoli, and A. Hartmann, "People detection and tracking with tof sensor," in *2008 IEEE Fifth International Conference on Advanced Video and Signal Based Surveillance*, pp. 356–361, Sep. 2008.

[37] O. Choi and S. Lee, "Wide range stereo time-of-flight camera," in *2012 19th IEEE International Conference on Image Processing*, pp. 557–560, Sep. 2012.

[38] M. Sallami and T. Zaharia, "Buildings detection from lidar data," in *2015 International Symposium on Consumer Electronics (ISCE)*, pp. 1–2, June 2015.

[39] S. Verghese, "Self-driving cars and lidar," in *2017 Conference on Lasers and Electro-Optics (CLEO)*, pp. 1–1, May 2017.

[40] M. Lobur, Y. Darnobyt, and R. Kryvyy, "Methods of car speed measurement based on doppler's effect," in *2011 11th International Conference The Experience of Designing and Application of CAD Systems in Microelectronics (CADSM)*, pp. 394–396, Feb 2011.

[41] Fan-Yi Lin and Jia-Ming Liu, "Chaotic lidar," *IEEE Journal of Selected Topics in Quantum Electronics*, vol. 10, pp. 991–997, Sep. 2004.

[42] X. Du, M. H. Ang, and D. Rus, "Car detection for autonomous vehicle: Lidar and vision fusion approach through deep learning framework," in *2017 IEEE/RSJ International Conference on Intelligent Robots and Systems (IROS)*, pp. 749–754, Sep. 2017.

[43] Chan Wei Hsu, Tsung Hua Hsu, and Kuang Jen Chang, "Implementation of car-following system using lidar detection," in *2012 12th International Conference on ITS Telecommunications*, pp. 165–169, Nov 2012.

[44] J. S. Schoenwald and E. D. McCullough, "Ultrasonic sensors for lunar and earth resource processing and manufacturing," in *1993 Proceedings IEEE Ultrasonics Symposium*, pp. 391–393 vol.1, Oct 1993.

[45] "Ultrasonic ranging module hc - sr04." `https://cdn.sparkfun.com/datasheets/Sensors/Proximity/HCSR04.pdf`. Accessed:01-October-2019.

[46] B. Christian, "Local discriminant bases and optimized wavelet to classify ultrasonic echoes: application to indoor mobile robotics," in *SENSORS, 2002 IEEE*, vol. 2, pp. 1654–1659 vol.2, June 2002.

[47] L. Kleeman and R. Kuc, "Mobile robot sonar for target localization and classification," *The International Journal of Robotics Research*, vol. 14, no. 4, pp. 295–318, 1995.

[48] M. E. Conde, S. Cruz, D. M. Muñoz, C. H. Llanos, and E. L. F. Fortaleza, "An efficient data fusion architecture for infrared and ultrasonic sensors, using fpga," in *2013 IEEE 4th Latin American Symposium on Circuits and Systems (LASCAS)*, pp. 1–4, Feb 2013.

[49] H. Furuhashi, Y. Uchida, and M. Shimizu, "Imaging sensor system using a composite ultrasonic array," in *SENSORS, 2009 IEEE*, pp. 1467–1472, Oct 2009.

[50] J. Lenz and S. Edelstein, "Magnetic sensors and their applications," *IEEE Sensors Journal*, vol. 6, pp. 631–649, June 2006.

[51] R. Kingman, S. C. Rowland, and S. Popescu, "An experimental observation of faraday's law of induction," *American Journal of Physics*, vol. 70, no. 6, pp. 595–598, 2002.

[52] F. Wu, L. Maréchal, A. Vibhute, S. Foong, G. S. Soh, and K. L. Wood, "A compact magnetic directional proximity sensor for spherical robots," in *2016 IEEE International Conference on Advanced Intelligent Mechatronics (AIM)*, pp. 1258–1264, July 2016.

[53] V. Genovese and A. M. Sabatini, "Differential compassing helps human–robot teams navigate in magnetically disturbed environments," *IEEE Sensors Journal*, vol. 6, pp. 1045–1046, Oct 2006.

[54] G. Nejat and B. Benhabib, "High-precision task-space sensing and guidance for autonomous robot localization," in *2003 IEEE International Conference on Robotics and Automation (Cat. No.03CH37422)*, vol. 1, pp. 1527–1532 vol.1, Sep. 2003.

[55] C. S. Meera, P. S. Sairam, and M. K. Gupta, "Path planning and motion control for a 3 dof massaging robot," in *2016 International Conference on Robotics and Automation for Humanitarian Applications (RAHA)*, pp. 1–6, Dec 2016.

[56] B. Scaglioni, N. Fornarelli, N. Garbin, A. Menciassi, and P. Valdastri, "Independent control of multiple degrees of freedom local magnetic actuators with magnetic cross-coupling compensation," *IEEE Robotics and Automation Letters*, vol. 3, pp. 3622–3629, Oct 2018.

[57] F. Xia, U. Zakia, C. Menon, and B. Bahreyni, "Improved capacitive proximity detection for conductive objects through target profile estimation," *Journal of Sensors*, 2019.

[58] F. Xia, F. Campi, and B. Bahreyni, "Tri-mode capacitive proximity detection towards improved safety in industrial robotics," *IEEE Sensors Journal*, vol. 18, pp. 5058–5066, June 2018.

[59] Z. M. Erickson, H. M. Clever, V. Gangaram, G. Turk, C. K. Liu, and C. C. Kemp, "Multidimensional capacitive sensing for robot-assisted dressing and bathing," *CoRR*, vol. abs/1904.02111, 2019.

[60] E. Zheng and Q. Wang, "Noncontact capacitive sensing-based locomotion transition recognition for amputees with robotic transtibial prostheses," *IEEE Transactions on Neural Systems and Rehabilitation Engineering*, vol. 25, pp. 161–170, Feb 2017.

[61] E. D. Kanygina, O. V. Denisova, and I. V. Rastvorova, "Optical and electrical control in printed circuit board manufacturing," in *2019 IEEE Conference of Russian Young Researchers in Electrical and Electronic Engineering (EIConRus)*, pp. 536–538, Jan 2019.

[62] B. Chen, Q. Wang, and L. Wang, "Adaptive slope walking with a robotic transtibial prosthesis based on volitional emg control," *IEEE/ASME Transactions on Mechatronics*, vol. 20, pp. 2146–2157, Oct 2015.

[63] "Capacitive micromachined ultrasonic transducers." `https://www.innovationservices.philips.com/looking-expertise/mems-micro-devices/mems-applications/capacitive-micromachined-ultrasonic-transducers-cmut/`. Accessed:01-October-2019.

[64] G. G. Yaralioglu, A. S. Ergun, Yongli Huang, and B. T. Khuri-Yakub, "Capacitive micromachined ultrasonic transducers for robotic sensing applications," in *Proceedings 2003 IEEE/RSJ International Conference on Intelligent Robots and Systems (IROS 2003) (Cat. No.03CH37453)*, vol. 3, pp. 2347–2352 vol.3, Oct 2003.

[65] R. Zhang, F. Gao, X. Feng, S. Liu, R. Ding, and Y. Zheng, "Photoacoustic resonance imaging," *IEEE Journal of Selected Topics in Quantum Electronics*, vol. 25, pp. 1–7, Jan 2019.

[66] T. Ma, S. R. Kothapalli, S. Vaithilingam, . Oralkan, A. Kamaya, I. O. Wygant, X. Zhuang, S. S. Gambhir, R. B. Jeffrey, and B. T. Khuri-Yakub, "3-d deep penetration photoacoustic imaging with a 2-d cmut array," in *2010 IEEE International Ultrasonics Symposium*, pp. 375–377, Oct 2010.

[67] H. Essen, S. Stanko, R. Sommer, W. Johannes, A. Wahlen, J. Wilcke, and S. Hantscher, "Millimetre wave sar for uav operation," in *Asia-Pacific Microwave Conference 2011*, pp. 963–966, Dec 2011.

[68] S. Clark and H. Durrant-Whyte, "Autonomous land vehicle navigation using millimeter wave radar," in *Proceedings. 1998 IEEE International Conference on Robotics and Automation (Cat. No.98CH36146)*, vol. 4, pp. 3697–3702 vol.4, May 1998.

[69] E. Abbott and D. Powell, "Land-vehicle navigation using gps," *Proceedings of the IEEE*, vol. 87, pp. 145–162, Jan 1999.

[70] S. Yang, W. Huang, and Q. Ma, "A method of genetic algorithm optimized extended kalman particle filter for nonlinear system state estimation," in *2009 Fifth International Conference on Natural Computation*, vol. 5, pp. 313–316, Aug 2009.

[71] J. Lien, N. Gillian, M. E. Karagozler, P. Amihood, C. Schwesig, E. Olson, H. Raja, and I. Poupyrev, "Soli: Ubiquitous gesture sensing with millimeter wave radar," *ACM Trans. Graph.*, vol. 35, pp. 142:1–142:19, July 2016.

[72] B. Bahreyni, "Vector light sensor and array thereof," 2015. US20160123803A1.

[73] A. B. Bhattacharyya, A. K. Tagore, and T. N. Basavaraj, "Silicon p-n junction photodiode characteristics with variable drift field in the diffused region," *Electronics Letters*, vol. 7, pp. 231–233, May 1971.

[74] L. Zhang, X. Zhao, Y. Fu, B. Xing, D. Yang, Q. Xu, Z. Ran, and X. Wang, "Computational design of optoelectronic semiconductor materials," in *2018 International Conference on Numerical Simulation of Optoelectronic Devices (NUSOD)*, pp. 37–38, Nov 2018.

[75] R. Xie, L. Mao, W. Guo, S. Xie, S. Zhang, L. Han, and F. Zhao, "High optical power density forward-biased silicon leds in standard cmos process," *IEEE Photonics Technology Letters*, vol. 27, pp. 121–124, Jan 2015.

[76] Xiangyi Guo, A. Beck, Bo Yang, and J. C. Campbell, "Low dark current 4h-sic avalanche photodiodes," *Electronics Letters*, vol. 39, pp. 1673–, Nov 2003.

[77] F. R. Quintela, R. C. Redondo, N. R. Melchor, and M. Redondo, "A general approach to kirchhoff's laws," *IEEE Transactions on Education*, vol. 52, pp. 273–278, May 2009.

[78] V. Suntharalingam, B. E. Burke, C. K. Chen, M. J. Cooper, and C. L. Keast, "Soi wafer selection for ccd/soi-cmos technology," in *2000 IEEE International SOI Conference. Proceedings (Cat. No.00CH37125)*, pp. 136–137, Oct 2000.

[79] A. Anusha, C. Parameswaran, P. Revathi, and V. Velmurugan, "Numerical simulation of dry and wet oxidation of silicon by tcad sprocess," in *International Conference on Advanced Nanomaterials Emerging Engineering Technologies*, pp. 513–516, July 2013.

[80] B. Stegemann, P. Balamou, T. Lussky, K. M. Gad, D. Vössing, M. Kasemann, and H. Angermann, "Passivation of crystalline silicon wafers by ultrathin oxide layers: Comparison of wet-chemical, plasma and thermal oxidation techniques," in *2018 IEEE 7th World Conference on Photovoltaic Energy Conversion (WCPEC) (A Joint Conference of 45th IEEE PVSC, 28th PVSEC 34th EU PVSEC)*, pp. 2779–2782, June 2018.

[81] Y. Tanabe, Y. Nakatsuka, S. Sakai, T. Miyazaki, and T. Nagahama, "Diluted wet oxidation: a novel technique for ultra thin gate oxide formation," in *1997 IEEE International Symposium on Semiconductor Manufacturing Conference Proceedings (Cat. No.97CH36023)*, pp. P49–P52, Oct 1997.

[82] M. A. Rosa, S. Dimitrijev, and H. B. Harrison, "Koh wet etching techniques for the micromachining of (100) soi wafers," in *1996 Conference on Optoelectronic and Microelectronic Materials and Devices. Proceedings*, pp. 454–457, Dec 1996.

[83] E. Herr and H. Baltes, "Koh etch rates of high-index planes from mechanically prepared silicon crystals," in *TRANSDUCERS '91: 1991 International Conference on Solid-State Sensors and Actuators. Digest of Technical Papers*, pp. 807–810, June 1991.

[84] K. Tokoro, D. Uchikawa, M. Shikida, and K. Sato, "Anisotropic etching properties of silicon in koh and tmah solutions," in *MHA'98. Proceedings of the 1998 International Symposium on Micromechatronics and Human Science. - Creation of New Industry - (Cat. No.98TH8388)*, pp. 65–70, Nov 1998.

[85] K. Sato, M. Shikida, Y. Matsushima, T. Yamashiro, K. Asaumi, Y. Iriye, and M. Yamamoto, "Characterization of anisotropic etching properties of single-crystal silicon: effects of koh concentration on etching profiles," in *Proceedings IEEE The Tenth Annual International Workshop on Micro Electro Mechanical Systems. An Investigation of Micro Structures, Sensors, Actuators, Machines and Robots*, pp. 406–411, Jan 1997.

[86] N. Inagaki, H. Sasaki, M. Shikida, and K. Sato, "Selective removal of micro-corrugation by anisotropic wet etching," in *TRANSDUCERS 2009 - 2009 International Solid-State Sensors, Actuators and Microsystems Conference*, pp. 1865–1868, June 2009.

[87] S. Qin, Z. Wang, Y. J. Hu, and A. McTeer, "Doping process for 3-d n-type trench transistors-2-d cross-sectional doping profiling study," *IEEE Transactions on Electron Devices*, vol. 60, pp. 2256–2260, July 2013.

[88] H. Hieber and K. Pape, "Lifetime of bonded contacts on thin film metallizations," in *22nd International Reliability Physics Symposium*, pp. 128–133, April 1984.

[89] W. J. Roesch and D. J. M. Hamada, "Correlating reliability to yield for liftoff metallization," in *2014 IEEE International Reliability Physics Symposium*, pp. 6C.1.1–6C.1.4, June 2014.

[90] "Photoresist az-703." `https://d3qi0qp55mx5f5.cloudfront.net/pnf/i/basic_pages/AZ_MIR_703_Photoresist_(19_cPs).pdf/`. Accessed:01-October-2019.

[91] M. Shikida, K. Sato, K. Tokoro, and D. Uchikawa, "Comparison of anisotropic etching properties between koh and tmah solutions," in *Technical Digest. IEEE International MEMS 99 Conference. Twelfth IEEE International Conference on Micro Electro Mechanical Systems (Cat. No.99CH36291)*, pp. 315–320, Jan 1999.

[92] "Coventorware." `https://www.coventor.com/mems-solutions/products/coventorware/`. Accessed:01-October-2019.

[93] I. El-chami, D. H. Zhuo, S. Vosoogh-Grayli, and B. Bahreyni, "A silicon vector light sensor for proximity sensing applications," in *2017 19th International Conference on Solid-State Sensors, Actuators and Microsystems (TRANSDUCERS)*, pp. 163–166, June 2017.

[94] R. F. W. Pease, "The scanning electron microscope," *IEEE Spectrum*, vol. 4, pp. 96–102, Oct 1967.

Appendix A

Calibration

In a no-light background, the light sensor has some small current flowing through it, this is dark current for the given sensor. It is possible to use software calibration to reduce this extra current as perceived by the sensor.

It is highly unlikely to have all diodes with identical characteristics, which makes it critical to subtract the difference in the actual and desired signal from the measured data. This difference - dark current - is subtracted from the input signal measured.

After successfully eliminating the extra current, and getting a mean of approximately $0V$ at the output across the photodiode, it is now possible to move on to the next step which is 'Angular Measurement' using the sensor.

The photodiodes used for light intensity measurement are placed on the pyramid side-walls as illustrated in figure A.1. These are opposite facing diodes as shown and are labeled as D_{East} and D_{West}.

Current flowing through the diode is given by equation:

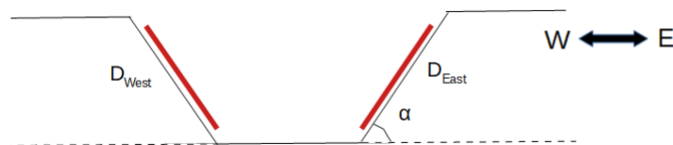$$I_d = I_0 \cdot \left(e^{\frac{qV}{nK_bT}} - 1 \right) + I_p$$

Figure A.1: Pyramid schematic with two independent photodiodes on the sidewalls

Figure A.2 illustrates an output voltage readout as recorded from D_{East} as recorded by the data acquisition system. More about the data acquisition system is discussed in 3.3.
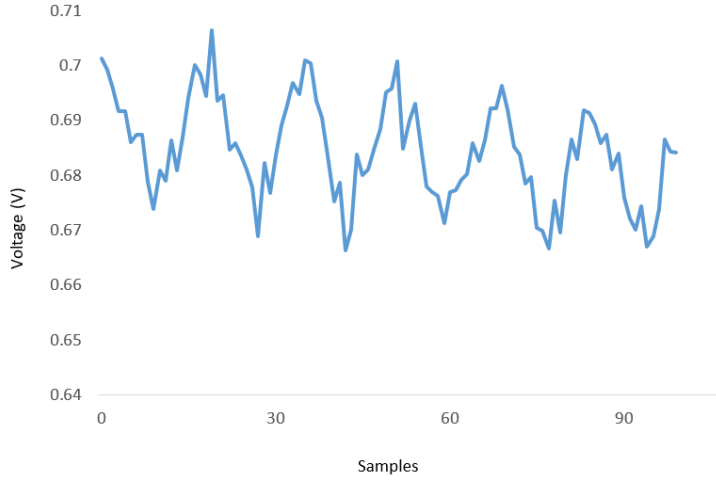
Figure A.2: Voltage output for D_{East} with incident light placed at $110°$ with respect to the sensor

Figure A.3 is data from the opposite photodiode in the same pyramid and it illustrates an output voltage readout as recorded in a similar manner from D_{West}. The power received on
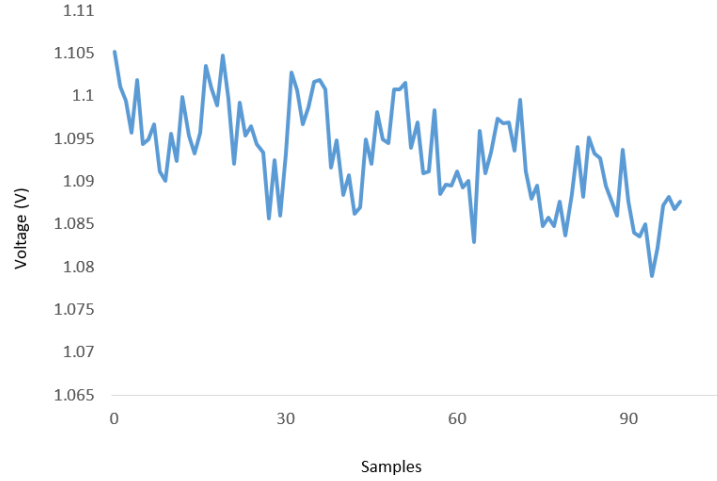

Figure A.3: Voltage output for D_{West} with incident light placed at $110°$ with respect to the sensor

the photodiode surface for D_{East} and D_{West} are:

$$P_{E_{incident}} = A_s \cdot \mathfrak{I}_{in} \cdot \sin(\beta + \alpha)$$
$$P_{W_{incident}} = A_s \cdot \mathfrak{I}_{in} \cdot \sin(\beta - \alpha)$$
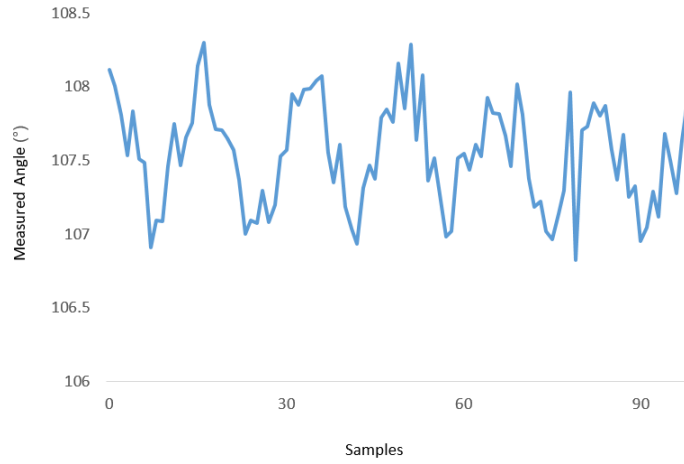
The ratio of power from light from East and West light sensors is given by:

$$R_{P_E/P_W} = \frac{\sin(\beta + \alpha)}{\sin(\beta - \alpha)}$$

63

The ratio is now used to measure the incident light angle β using:

$$\beta = \alpha - \arctan\left(\frac{R_{P_E/P_W} \cdot \cos(2\alpha) - 1}{R_{P_E/P_W} \cdot \sin(2\alpha)}\right)$$

Finally, the desired angle is estimated and the results are as shown in figure A.4.

Figure A.4: Calculated angular measurement using D_{East} and D_{West} intensity values